Design and Fabrication of a Novel Corner Wheel Module for Urban Vehicles

by

Mohammad-Amin Rajaie

A thesis
presented to the University of Waterloo
in fulfillment of the
thesis requirement for the degree of
Master of Applied Sience
in
Mechanical Engineering

Waterloo, Ontario, Canada, 2016

AUTHOR'S DECLARATION

I hereby declare that I am the sole author of this thesis. This is a true copy of the thesis, including any required final revisions, as accepted by my examiners.

I understand that my thesis may be made electronically available to the public.

Abstract

This thesis proposes a new design of corner wheel modules for narrow vehicles. Independent corner wheel modules with integrated powertrain, suspension, steering, and camber mechanisms combined with x-by-wire technology can replace engines, mechanical linkages, and drive shafts in vehicles. The integration of such components in the corner module creates extra room that can be used for passenger comfort. The proposed module is especially appropriate for small and narrow vehicles where packaging of all vehicle subsystems is a demanding task. It also significantly simplifies the complex chassis design and assembly process of vehicles.

The new concept introduced in this thesis utilizes a four-bar linkage as the steering mechanism for the first time. This corner module also incorporates another four-bar mechanism to provide active camber control for the wheel. It is shown how an active camber control considerably improves the rollover threshold of narrow vehicles. The combination of these two four-bar mechanisms results in a virtual kingpin axis that provides stability for the chassis system. This approach results in a highly compact design for the corner module that can be integrated into narrow vehicles.

The feasibility of the kinematic design, mechanical design, and stress analysis is confirmed by fabricating a full sized prototype. This prototype was tested in the laboratory environment and verified the simulation results presented in this thesis. The prototype also showed that the new design is easy to assemble for manufacturing purposes and more importantly this module can easily be maintained during its life time.

Acknowledgements

I would like to truly thank my supervisor Professor Amir Khajepour for all his guidance and support as well as his endless patience throughout my masters' research. In a sentence, it was an honor to work under his supervision.

I would also like to thank Dr. Alireza Pazouki whose support and guidance constantly helped me during my master's project.

Dedication

I would like to dedicate this thesis work to my father, who has always been the greatest source of encouragement and support throughout my life, and to my mother, who always loves me unconditionally.

Table of Contents

List of Figures

List of Tables

Chapter 1
Introduction

Space limitation and traffic congestion are two of the major growing problems in urban areas worldwide. The population of urban areas is estimated to increase form 3.4 billion in 2010 to 6.4 billion in 2050 [1] . Moreover, the number of vehicles is rapidly increasing and is expected to reach nearly 2 billion by 2050 while the number of main roads remains approximately the same in large cities [2]. In addition to space limitation and traffic congestion, other concerns such as fuel consumption and environmental aspects of vehicles are rising amongst governments.

Electric urban vehicles seem like a viable solution to alleviate the abovementioned concerns [3]. Urban vehicles or micro-cars are smaller in size compared to average passenger cars and they are generally used for urban commuting. Since the average vehicle occupancy is about 1.67 [4] persons per car, these cars are usually designed for two passengers. Electric urban vehicles are more efficient in terms of energy consumption and greatly reduce vehicles' pollutions in urban areas. Furthermore, due to their small sizes, using these vehicles would result in denser parking and lane splitting; ergo less traffic and lower emission. Driving urban vehicles is also appealing because of their ease of navigation in cluttered areas and their high maneuverability.

Despite of these benefits, urban vehicles are not fully accepted by the market yet. Current urban vehicles do not demonstrate a high ride quality. More importantly their small and confined passenger compartments are not comfortable for passengers; hence, there is minor customer approval. These problems are due to the fact that most of the current urban vehicles are designed as scaled down versions of passenger cars. For example, these vehicles are designed with their powertrain and suspension external to the wheels similar to conventional passenger cars. This approach requires a significant volume dedicated for the mechanical linkages used for transferring power and load.

It is feasible to integrate suspension and powertrain into the wheel module. Moreover, utilizing x-by-wire (Drive-by-wire, brake-by-wire, steer-by-wire and camber-by-wire) technology can replace all the mechanical linkages, which results in lighter cars with lower energy consumption. Consequently, this extra volume generated by eliminating linkages can be used for passenger comfort. This approach leads to the idea of having a wheel corner module.

A wheel corner module is integrated with powertrain, suspension, braking, camber, and steering systems combined with x-by-wire technology. Each compact module is installed at a corner of the vehicle and is controlled independently from other modules. Therefore, there is more control over the

dynamics of the vehicle as a whole through independent torque vectoring and active steering of each wheel.

The purpose of this thesis is to perform design, optimization, fabrication, and experimental analysis of a new wheel corner module for urban vehicles.

In Chapter 2, a study is conducted on existing corner module concepts and designs previously introduced in the literature by industry. In Chapter 3, a thorough kinematic analysis is performed on the dual four-bar mechanisms for the proposed corner module. The preliminary outcome of this analysis is the location of the hard points for the mechanisms. The locations of these points are subjected to predefined packaging constraints. Moreover, these hard points are determined in a way that steering and camber requirements are met.

Chapter 4 studies ride comfort and rollover behavior of a three-wheeled tadpole vehicle with the corner module. Suspension stiffness is determined based on ride quality for a quarter car model. Through an iterative process, this stiffness is improved until it satisfies both ride quality and roll gain requirements. The effect of camber is studied on rollover behavior of the vehicle. Then, it is presented how cambering of wheels can improve the rollover threshold of narrow vehicles.

Chapter 5 is dedicated to detailed design and stress analysis of the corner module. The shape of each member is designed to avoid internal collision with other members during steering and cambering. The mechanical design of the entire module is discussed in details and stress analysis is implemented on the model. Based on the stress analysis an appropriate material is selected to withstand yielding.

Chapter 6 explains fabrication procedure and experimental validation of the corner module that was conducted through this research. A test fixture is designed in order to carry out various tests on the corner module. Data acquisition methods are selected and discussed. The results are presented at the end of chapter 6. In chapter 7, an optimization method is proposed that can be utilized in the future and improve the performance of the design. The results of the optimized design is compared with the proposed design in this thesis.

In the last chapter, Chapter 8, conclusion of the thesis is covered and recommendations for future works are made.

Chapter 2
Literature Review

This chapter studies some of the existing corner module concepts in the literature and market. Most of these corner wheel modules are designed to simplify the chassis design and assembly of vehicles. In general, design of electric vehicles is more flexible than vehicles with internal combustion engines. This is due to the fact that energy and power can be transferred via flexible wires rather than rigid shafts. The idea of utilizing a corner module combined with x-by-wire technology increases this flexibility further by eliminating steering and suspension links. Significantly reduced number of mechanical linkages and drive shafts results in lighter, more spacious, and more efficient vehicles. In addition to simpler assembly process and reduced cost, these independent modules can greatly help with stabilizing the vehicles. These modules can generate independent torques and steering angles to better stabilize the vehicle compared to conventional cars. This feature increases the safety of vehicles and passengers. Based on the abovementioned benefits, many car and tire manufacturers have started developing corner wheel modules which are studied in this chapter. At the end of this chapter the shortcomings of these designs are addressed and a new mechanism based design with higher performance is proposed. The proposed design approach is highly suitable for narrow urban vehicles and improves many of the shortcomings of existing designs.

2.1 Michelin Active Wheel [5]

Michelin introduced the Active Wheel in 2004 at the challenge Bibendum and later implemented this concept on the Heuliez Will in 2008. This wheel comprises of water cooled electric in wheel motor that provides traction for the wheel. The difference between this concept and other in wheel motors is the use of pinion and gearwheel which transfer the torque of the motor to the hub. As a result, a smaller motor can be used to drive the wheel which reduces the un-sprung mass and improves ride quality of the vehicle; thus, a more compact design is achievable. This wheel also has a built-in active suspension system. This suspension system includes a passive coil spring and an active electric actuator that isolate the chassis from low and high frequency vibrations induced by the road. There is also a conventional brake caliper coupled with a brake disk to assist with the regenerative braking as necessary [6]. This wheel is depicted in Figure 2-1.

Figure 2-1: Michelin active wheel [7]

This in wheel suspension system is patented by Michelin [8] which also allows for connecting a rod to change the camber angle of the wheel as shown in Figure 2-2.

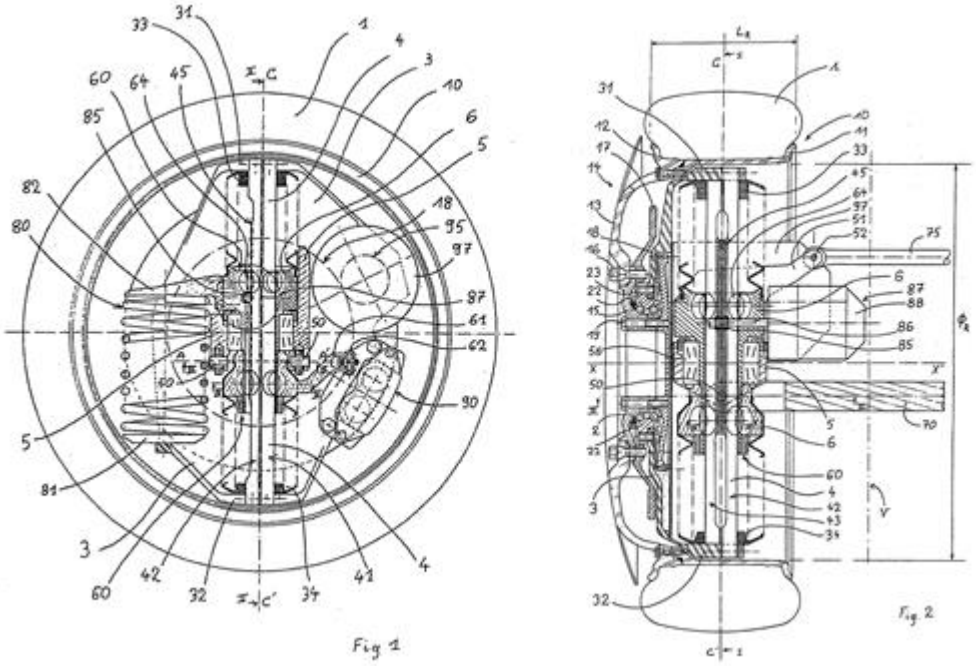

Figure 2-2: Wheel assembly a suspension integrated in the wheel hub [8]

Michelin also has a patent on active camber control [9] for this module. The proposed cambering mechanism can provide high camber angles up to 15 degrees in each direction. However, implementing this mechanism contradicts with the compact design of the active wheel as illustrated in Figure 2-3. Therefore, the implementation of this feature was never demonstrated on this system.

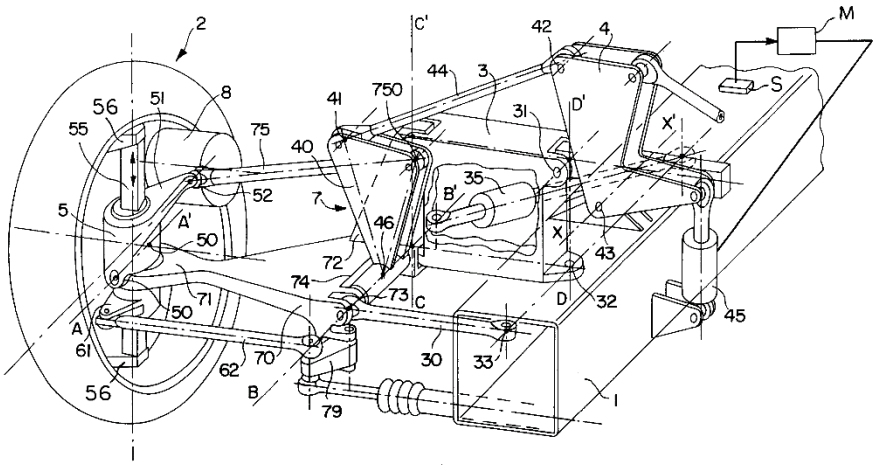

Figure 2-3: Vehicle suspension having active camber [9]

Steering mechanism for this module is also based on conventional steering linkages. This linkage can also be replaced by an actuator connected to the body.

2.2 Siemens e-Corner

Siemens developed the same concept called e-Corner, which was sold to Continental in 2007. This design contains more components in one module and it is more compact than Michelin Active Wheel. It also removes the need for conventional steering linkage and braking system [10] as opposed to Michelin Active Wheel. The e-Corner, presented in Figure 2-4, includes a direct in-wheel motor for its drive and an in-wheel suspension at the center of its wheel. By using the patent on brake systems [11], electronic wedge brake system eliminates the need for conventional brake systems. Moreover, e-Corner utilizes a very compact steering mechanism. However, the steering mechanism is still in the conceptual phase and it is under development and no working prototype of the steering has been demonstrated yet. Moreover, this module cannot provide any camber angle for the wheels which is considered as one of its shortcomings. Furthermore, the un-sprung mass of this module is still unknown since it is still in the concept phase.

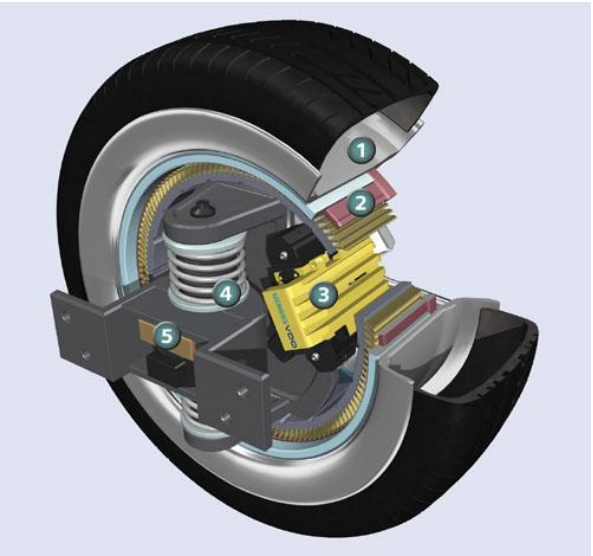

Figure 2-4: Siemens e-Corner [10]

2.3 Hiriko Robo-Wheel

Hiriko is a foldable city car that greatly helps with the parking issue in large cities. The foldable chassis for this vehicle is demonstrated in Figure 2-5, and Figure 2-6 shows how passengers can get off the vehicle through the front door. The concept was initially developed at MIT media lab in 2003 and the project was shut down in 2015 due to some legal issues. Because the design of the car is highly compact, there was a need for a corner module to satisfy packaging requirements. Robo-wheel [12] shown in Figure 2-7 was developed for this vehicle based on patented robot wheel by MIT [13] which is integrated with in-wheel motor in addition to steering, suspension, and brake systems as depicted in Figure 2-8. This module is much heavier than other concepts; however, the speed of the vehicle is self-limited to 50 km/h. Therefore, the ride comfort of this vehicle is not an issue at these speeds. Furthermore, the angled kingpin axis for this module makes it more stable than other concepts. On the other hand, this module is incapable of cambering. The wheel track of this vehicle is 1.5 m; hence, it is not considered as highly narrow vehicle and lack of camber is insignificant.

Figure 2-5: Hiriki foldable chassis [12]

Figure 2-6: Hiriki folds for parking purposes [12]

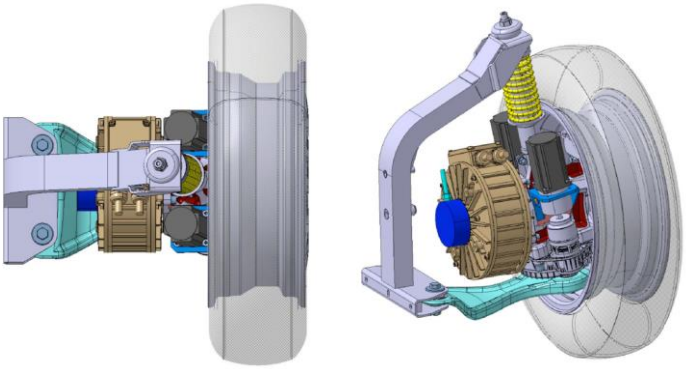

Figure 2-7: Hiriki robor-wheel [12]

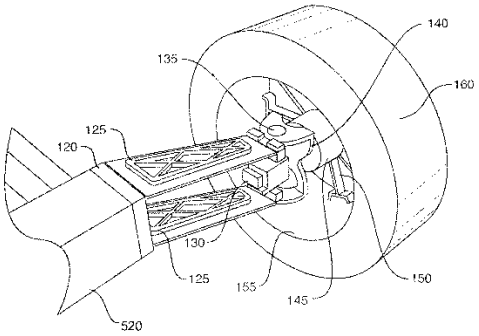

FIG. 2

Figure 2-8: MIT robotic wheel [13]

2.4 NASA e-Corner

In 2013, NASA showcased its new modular robotic vehicle (MRV) which utilizes the mars rover technology in its chassis and chassis system designs as demonstrated in Figure 2-9 [14]. NASA claims this vehicle can be used as an urban vehicle with ultimate maneuverability [15]. This vehicle uses a fully electric corner module which is capable of steering 180 degrees using an electric motor on top of the module. This module utilizes a passive suspension mechanism. Using NASA's E-corner at four corners of the vehicle provides high stability and maneuverability for the car.

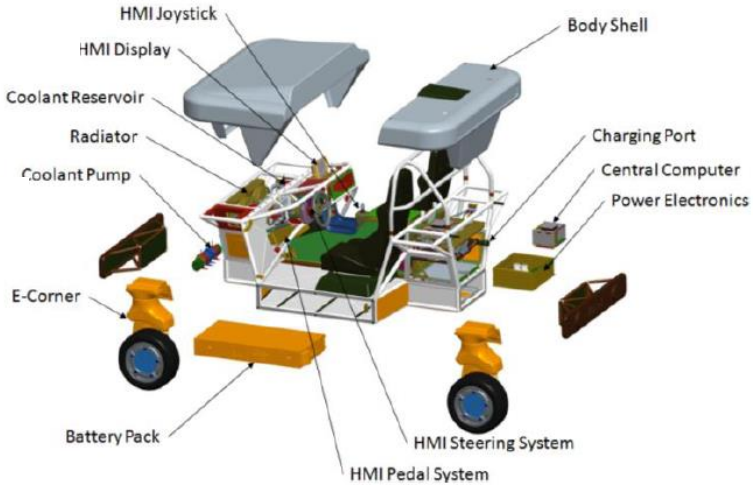

Figure 2-9: NASA modular robotic vehicle sub-assemblies [14]

This module uses x-by-wire technology to eliminate the need for extra shafts and links as well as hydraulic equipment for brake systems. The NASA E-corner is depicted in Figure 2-10 where it is installed on the vehicle.

Figure 2-10: NASA MRV E-corner [15]

Figure 2-11: NASA MRV wheels can rotate 180 degrees which provides ultimate stability and maneuverability for the vehicle [14]

As demonstrated in Figure 2-11, MRV's wheels can rotate 180 degrees which enables this vehicle to move sideways as well as do a full rotation about its center which greatly helps with parking ability of the vehicle. Even though this module is fully controllable, the amount of space it requires exceeds the provided space for corner modules in most of narrow urban vehicles. This relatively large size of the module is considered as one of its limitations for urban vehicles use.

2.5 Volvo Autonomous Corner Module

In 1998, Volvo patented [16] its corner module for passenger vehicles which is demonstrated in Figure 2-12. This corner module includes an active suspension, active camber and an innovative steering mechanism in addition to its in-wheel motor with integrated friction brake system. Figure 2-13and Figure 2-14 demonstrate the side view and top view of this module [17]. These figures show how the camber mechanism is integrated with suspension mechanism. Moreover, utilization of two synchronized actuators together as the steering mechanism reduces the size of these actuators which results in a more compact design of the autonomous corner module.

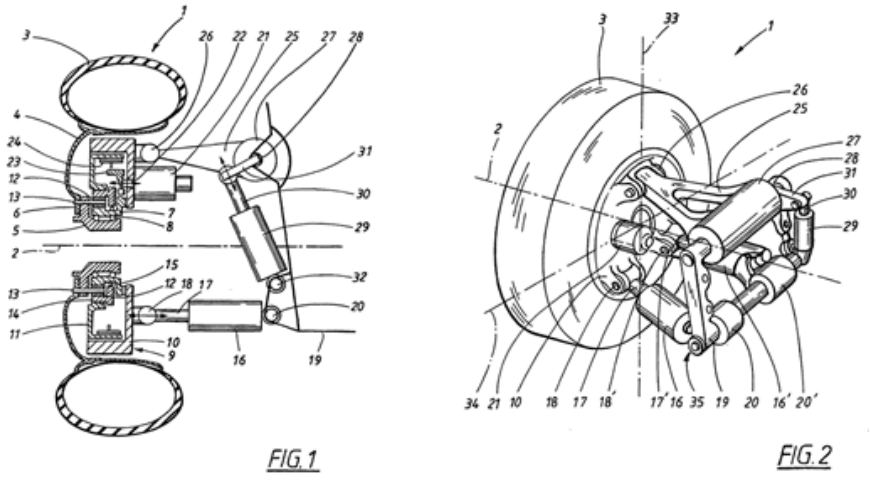

Figure 2-12: Volvo corner module patent [16]

The embodiment of this patent was proposed by Sigvard Zeterstrom owner of the patent as well and it was called the autonomous corner module. This is the most complete corner module design compared to other concepts. This wheel satisfies steering angles up to 22 degrees in each direction.

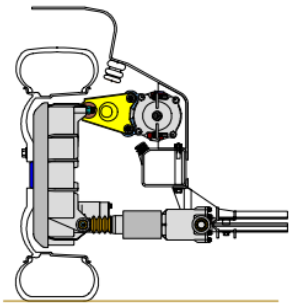

Figure 2-13: Volvo autonomous corner module side view, camber and suspension mechanism [17]

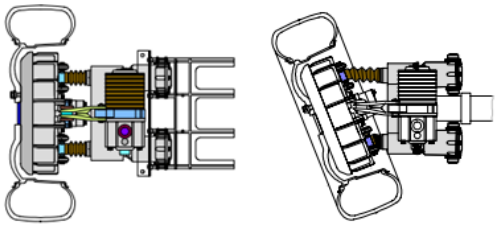

Figure 2-14: Volvo autonomous corner module top view, steering mechanism [17]

2.6 Proposed Corner Module

As it was briefly discussed in this chapter, the existing corner modules have some shortcomings that are addressed in this section.

Incorporating a steering mechanism into the corner module has been a challenging task for the current designs. Some of these modules use conventional steering linkages which contradict with the idea of having independent corner modules. NASA utilizes an electric motor for its steering purposes which is quite large and do not meet the packaging requirements of many small vehicles. Moreover, Volvo utilizes a dual actuator mechanism which significantly adds to the cost of manufacturing and the controller electronics of this module.

Furthermore, most of the mentioned corner modules do not provide active camber mechanism. This feature can be used to greatly improve the rollover threshold of narrow vehicles. Narrow vehicles are highly prone to rollover and they need a mechanism to prevent this behavior. None of the abovementioned modules provide this active camber mechanism in their corner modules and instead reduced the operating speed of their vehicles or used conventional anti-roll bars.

This thesis proposes a new corner module design in which for the first time introduces a four-bar mechanism whose motion is over-constrained by a linear actuator to function as the steering mechanism. This mechanism can satisfy steering requirements. In addition, using four-bar mechanism helps to reduce the amount of forces on the steering actuator; as a consequence, smaller actuator can be selected to serve for steering purposes. Moreover, another four-bar linkage is integrated with the suspension system to provide high camber angles for the wheel. The combination of these two mechanisms creates a virtual kingpin axis that can help to passively stabilize the chassis system as well. This mechanism results in a highly compact design that can be implemented in small vehicles.

Chapter 3
Design and Analysis of the Corner Module

The proposed corner module in this thesis is going to be implemented on a three-wheeled narrow urban vehicle. Complete control over each wheel corner module can improve the stability of the vehicle up to a point that having only three wheels can satisfy the stability requirements of urban vehicles. Thus, smaller and lighter power sources, such as hydraulic pumps for steering and braking, can be utilized in the vehicle to run three wheel corner modules as opposed to four. Therefore, the vehicle is lighter, more spacious and more efficient. In addition, the cost of the vehicle is lowered. High efficiency, high comfort level, and low cost are appealing to costumers and generate a much higher market acceptance. Because of lower energy consumption and lower emission, three-wheelers are gaining more attention around the world. For instance, some three-wheeled cars are already being used in some populous cities in India and China. In general, three-wheeled vehicles come in two different configurations, delta and tadpole. Having two wheels at the back and one in front is known as the "delta" configuration. The benefit of this setup is its low cost. Opposite of the delta configuration is called "Tadpole" configuration with two wheels up front and one at the back. Tadpole design has more understeering tendency, therefore, is more stable than the delta configuration at high speeds. Moreover, the Tadpole design is highly aerodynamic due to its tear drop shape.

As a result, this module should meet all the requirements for the three wheeled vehicle. This three-wheeled vehicle is smaller and narrower than Smart Fortwo; therefore, requires a highly compact corner module. This chapter investigates the packaging constraints and steering requirements for the corner module. Furthermore, based on these requirements the kinematics for the steering mechanism and camber mechanism is studied and investigated using a numerical approach. The outcome of the study in this chapter is to determine the locations of the hard points for the corner module mechanisms.

The combination of these two mechanisms results in a virtual kingpin axis. Hence, a method is proposed to define this kingpin axis for the wheel. The effect of the kingpin axis in both conventional chassis systems and the proposed corner module is investigated and discussed.

3.1 Dimensional Requirements

The wheel corner module has to be designed within the geometric boundaries of a conventional wheel. As a result, serious spatial limitations are imposed on the location of hard points and length of each member. Based on packaging requirements, an envelope has been defined for the steering mechanism,

suspension mechanism, camber mechanism, and their actuators as depicted in Figure 3-1. The dimensions of this box are 30x60x67 cm^3. This envelope ensures the corner module fits in its predefined location on the chassis of the three-wheeled vehicle as demonstrated in Figure 3-1. Yet enough room is dedicated for the battery pack and hydraulic components of the vehicle.

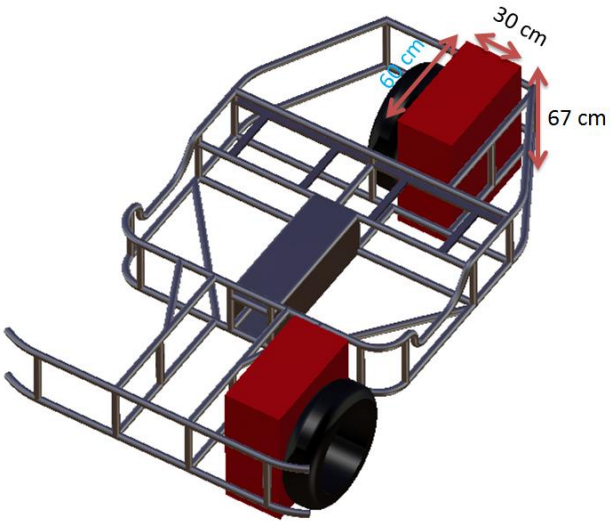

Figure 3-1: Restricted predefined packaging area for the corner module

3.2 Maximum Steering Angle

The maximum steering angle is defined based on minimum turning radius of the vehicle. Smaller turning radius indicates better parking ability and higher maneuverability of the vehicle in cluttered areas. In this section, the maximum steering angle for the urban vehicle is determined.

Employing wheel corner module gives the ability to steer each wheel, including rear wheels, independently. Hence, rear steering can greatly help to decrease turning radius. Since the minimum turning radius is only for parking purposes, vehicle speeds are very low and tires' side-slip angles are close to zero [18]. In other worlds, tires' direction of heading and its direction of travel are the same. This fact helps to accept that the direction of velocity for each wheel is the same as its direction of heading at maximum steering angles.

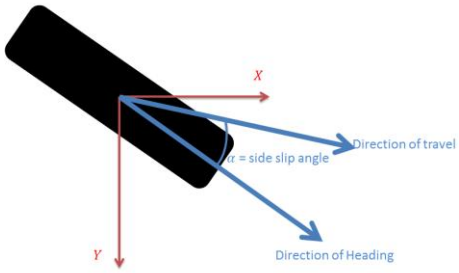

Figure 3-2: Tire side slip angle is the angle between tires direction of heading and its direction of travel.

Moreover, the instantaneous center of rotation of the vehicle at low speeds can be found using the wheels and body kinematics. Instantaneous center of rotation of a rigid body is the point on the body where its velocity is zero. Each point on the rigid body rotates about the instantaneous center of rotation with the same angular velocity ω. As a result, the velocity of each point is perpendicular to line connecting the point to the instantaneous center of rotation.

Two points on the body with known velocity directions can be used to find the instantaneous center of rotation. Taking the graphical approach, the direction of velocities of inner front tire and the rear tire are determined based on their maximum steering angle. The radii of curvature for these points are two lines perpendicular to these velocities. Consequently, the intersection of these two points determines the location of instantaneous center of rotation of the car. This is called the Ackermann principle [19]. Curb to curb turning circle is twice the distance between the outer wheel of the vehicle and the instantaneous center of rotation. As depicted in Figure 3-3, it can be observed that when the inner front wheel and the rear wheel are steered to their maximums in opposite directions, the turning radius R is minimums.

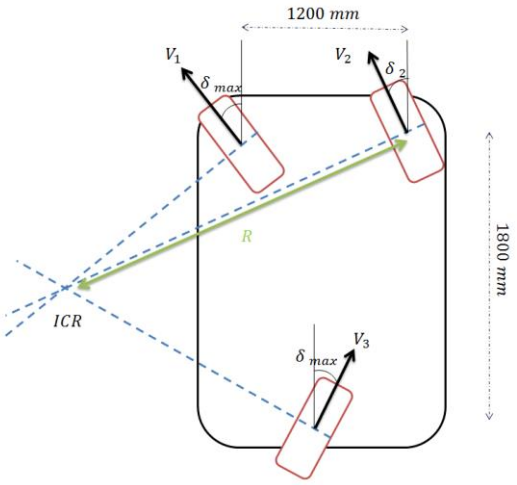

Figure 3-3: Three wheeled vehicle instantaneous center of rotation

Taking graphical approach it can be calculated that for developing the three wheeled vehicle the minimum curb to curb turning circle is 6.928 meters with maximum 20 degrees of steering angle for each wheel. Today the record for curb to curb turning circle belongs to Smart Fortwo with 6.95 meters. Thus, the requirement for maximum steering angle is set to be 20 degrees in each direction.

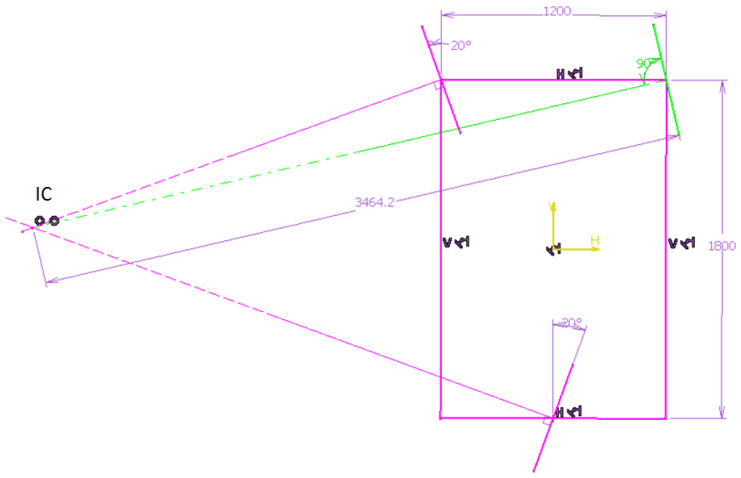

Figure 3-4: Graphical approach to measure curb to curb turning circle

3.3 Configuration of Steering and Camber Mechanisms

The entire mechanism configuration for the wheel corner module consists of a dual four-bar linkage as illustrated in Figure 3-6. The first one is the camber mechanism QDH_2E, which is connected to the chassis through points D and E through revolute joints. Link EH_2 is a linear actuator with variable length. The change in length of actuator EH_2 results in changing the angle of plane ABP which can freely rotate about line AB and is rigidly connected to the wheel. As a result, the camber angle of the wheel changes by changing the length of the actuator. Camber angle is the angle that wheel creates with the plane normal to the ground as depicted in Figure 3-6. The importance of this parameter and its effect on vehicle dynamic is discussed later in chapter 4.

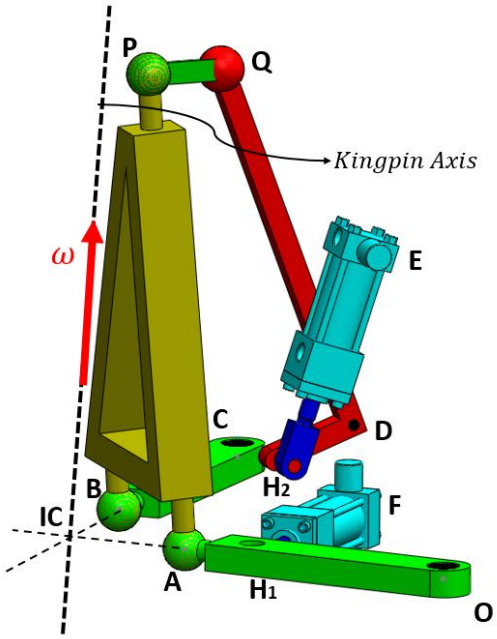

Figure 3-5: Proposed dual four-bar linkage schematics for the corner module steering and camber mechanisms

The second mechanism is a planar four-bar mechanism OABC connected to the chassis through points O and C by revolute joints. Link OA is connected to linear actuator FH_1 at point H_1. Hence, any change in the length of the actuator results in change of the angles of the four-bar mechanism. Since the wheel is connected to plane ABP, it can be concluded that the angle of link AB with line OC is the same as the steering angle for the wheel.

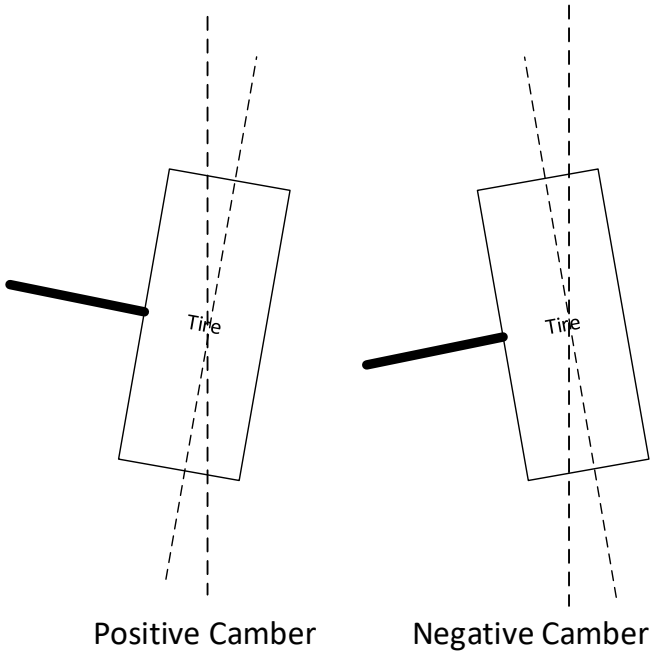

Figure 3-6: .Vehicle front view. Side view of wheel and its camber angle

3.4 Kingpin Axis

The combination of the two steering and camber mechanisms results in having a virtual kingpin axis for the wheel. Thus, by using these four-bar linkages, a very compact design can be achieved that meets all the requirements for the chassis system.

The kingpin axis is the axis of rotation of the wheel at any instance. Because the wheel is rigidly connected to plane ABP, it can be said that the axis of rotation for plane ABP is the same as the kingpin axis.

In order to find instantaneous axis of rotation of body ABP, Chasles' theorem [20] is employed. According to Chasles' theorem the motion of a rigid body at any instance can be considered as superposition of a rotation ω about an axis and a velocity v parallel to this axis. This axis is called instantaneous axis of rotation of the body.

The first step is to find the direction of angular velocity of the body ω at any instance. This rotation vector determines the direction of the instantaneous axis of rotation. Furthermore, one point on this axis must be determined. By having one point and the direction, the line can be defined. The instantaneous center of rotation of any point of the rigid body, lies on the instantaneous axis of rotation as well. Using

this fact, it is guaranteed that the instantaneous center of rotation of link AB always lies on the axis of rotation of rigid body ABP.

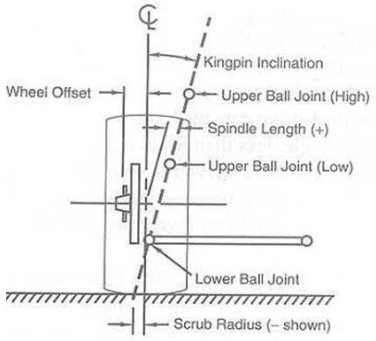

Figure 3-7: Kingpin axis is the axis that the wheel rotates about during steering and camber [21]

The fact that link AB is part of planar four-bar linkage OABC helps to find its instantaneous axis of rotation in a straightforward manner. Since this link is restricted to move in one plane, it makes a special case and it only rotates about the intersection of its instantaneous axis of rotation and the plane it moves on. This intersection point for this special case is called the instantaneous center of rotation of the body. To find the instantaneous center of rotation of link AB the kinematic principles for rigid body motion are used. These principles lead to the fact that the linear velocity of each point on the rigid body is perpendicular to its radius of rotation [22].

In the four-bar linkage, link OA rotates about point O and link CB rotates about point C. Their velocities, V_A and V_B, are determined graphically, as depicted in Figure 3-8, where they are perpendicular to links AO and CB. Afterwards, the rigid link AB should be considered, where velocities of points A and B can be used to find radii of rotations in rigid link AB. Since all radii of rotation go through the instantaneous center of rotation, this point can simply be found by intersecting perpendicular lines to V_B and V_A. It is worth to note that these lines are the same as lines AO and BC.

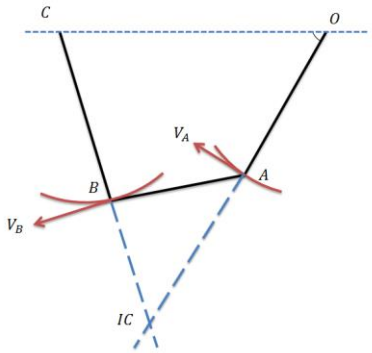

Figure 3-8: Instantaneous center of rotation for the coupler of a four-bar linkage mechanism

Moreover, angular velocity of rigid body ABP can be calculated using velocities of points P and A. By solving the geometry at any time, velocity vectors of points P and A, and their relative position vector $r_{P/A}$ can be calculated. Therefore, the angular velocity ω can be determined when dt approaches zero:

$$V_P = V_A + \omega_{ABP} \times r_{P/A} \rightarrow \frac{dr_P}{dt} = \frac{dr_A}{dt} + \frac{d\theta_{ABP}}{dt} \times r_{P/A} \rightarrow dr_P = dr_A + d\theta_{ABP} \times r_{P/A} \quad (3\text{-}1)$$

Equation (3-1) is in vector form and provides three equations to find the three components of $d\theta_{ABP}$. $d\theta_{ABP}$ determines the direction of angular velocity of the rigid body when dr_P and dr_A approach zero. By applying a small change in the length of the steering actuator and solving the geometry for its new configuration the value of $d\theta_{ABP}$ can be found.

Having the location of instantaneous center of rotation of link AB, (x_{IC}, y_{IC}, z_{IC}) and the direction of angular velocity $d\theta_{ABP}$ of body ABP, $(d\theta_{ABPX}, d\theta_{ABPY}, d\theta_{ABPZ})$ defines the equation of line for axis of rotation:

$$\frac{x - x_{IC}}{d\theta_{ABPX}} = \frac{y - y_{IC}}{d\theta_{ABPY}} = \frac{z - z_{IC}}{d\theta_{ABPZ}} \quad (3\text{-}2)$$

3.5 Effects of Kingpin Axis

In designing conventional steering systems, kingpin axis plays a major role. Two of the most important effects of kingpin axis are creation of scrub radius and mechanical trail. As it is depicted in Figure 3-7, scrub radius is the lateral distance between the contact patch center of the tire and the point of

intersection of the kingpin axis with the ground. Where, mechanical trail is the longitudinal distance between these two points. These values have to be designed carefully to provide a stable chassis system as discussed in sections 3.5.1 and 3.5.2.

3.5.1 Scrub Radius

In conventional steering systems, scrub radius can cause the "toe" phenomenon. Toe-in and toe-out happen when the front wheels point towards opposite directions. This affects the dynamic of the vehicle [23]. In order to minimize this effect, the steering link must have very small compliance and be very stiff to resist any deformation. However, there is always compliance in the system due to the existence of rubber bushings and tires.

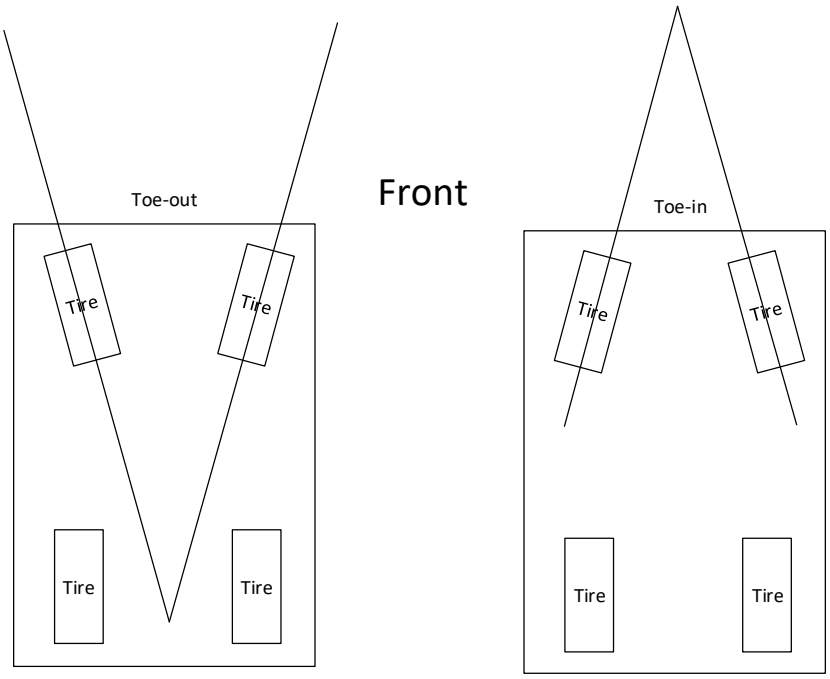

Figure 3-9: Toe phenomenon happens when front wheels of the car rotate towards opposite directions.

The toe phenomenon happens due to longitudinal forces of the tires which create a moment about their center of rotation resulted from the kingpin axis. Based on the value and location of scrub radius, the toe-in and toe-out behavior change during braking and accelerating as depicted in Figure 3-10 and Figure 3-11.

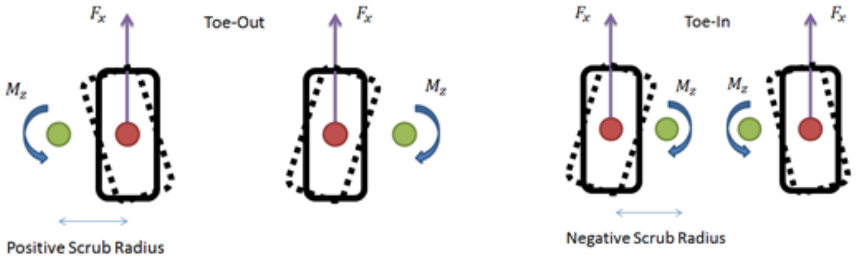

Figure 3-10: Effect of scrub radius location on toe phenomenon during acceleration on front tires. Red point is the contact patch of the tire and green point is the center of rotation of the tire.

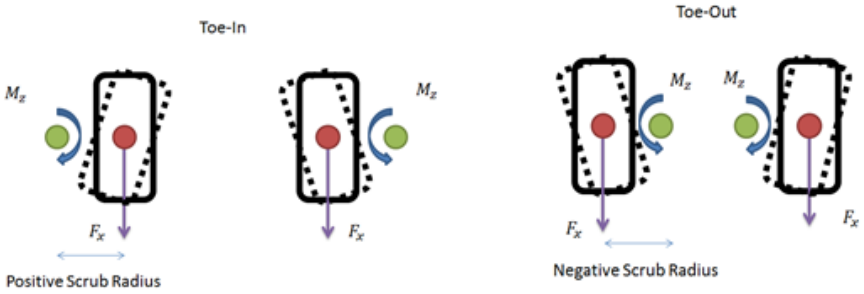

Figure 3-11: Effect of scrub radius location on toe phenomenon during braking on front tires. Red point is the contact patch of the tire and green point is the center of rotation of the tire.

Longitudinal forces of the tires create a moment on the wheel about the kingpin axis. However, in conventional steering systems where both right and left wheels are connected by the steering mechanism, the toe-in and toe-out effects are minimal. Because any rotation in one wheel is transferred to the other wheel, through rigid steering links, and causes a rotation in the same direction as the first wheel; therefore, it counter acts with toe-in and to-out phenomena where both wheels are rotated in opposite directions. In the case of independent corner modules, each wheel is steered independently and there is no mechanical linkage between the wheels. As a result, this phenomenon has to be controlled by the actuators instead of the steering links. Active actuators can compensate for the toe phenomenon. Furthermore, actuators have to be able to handle high loads. As a result, the value of scrub radius should be highly considered for force analysis to select right actuators to actively control of the toe [24].

3.5.2 Mechanical Trail

For conventional steering systems, mechanical trail provides directional stability [25]. When the wheels are steered, a lateral force is created on tires. If the instantaneous center of rotation of the tire is in front of tires' contact patch, lateral disturbance forces create a moment that rotates the wheels back to their straight position. This can also reduce the steering effort by driver to correct the steering after a sharp turn. Therefore, any disturbance on the wheels automatically gets corrected by having a positive mechanical trail. On the other hand, negative mechanical trail causes more disturbances on the wheels and makes the vehicle more unstable. In the case of the corner module, the length of the actuators are fixed unless the driver sends a command; therefore, fixed actuators resist the road disturbances and as a result the self-aligning moment. As a consequence, for steer-by-wire systems mechanical trail does not have the same significance on the design as conventional systems and instead an intelligent control system has to be implemented to correct the wheels' orientations by sending the right commands to the actuators. In case of any failure in the actuator, a positive mechanical trail however, would be beneficial.

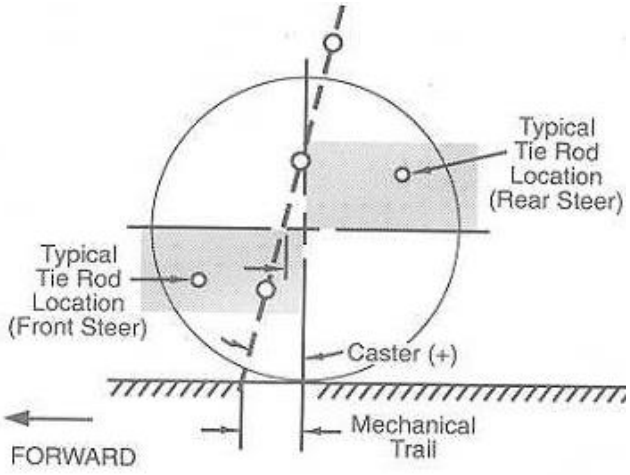

Figure 3-12: Effect of caster angle of the kingpin axis to create mechanical trail [21]

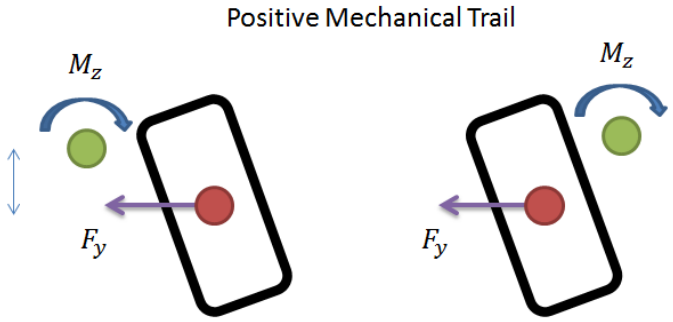

Figure 3-13: Positive mechanical trail provides directional stability for the car, where lateral forces rotate the wheels back to their straight orientation.

It can be concluded, that the kingpin axis does not play a major role in stabilizing corner modules as opposed to conventional chassis systems. However, this parameter affects the amount of forces that actuators have to bear. As a result, it is helpful to consider this parameter in the design as well.

3.6 Location of Mechanisms Hard Points

The dual four-bar mechanism must be designed in an optimal manner to meet all the above mentioned requirements and constraints. In order to achieve this goal a geometric approach is undertaken. First, the equations are derived in a parametric form. Later, the spatial locations of hard points are selected manually using engineering judgment within the geometric constraints in order to meet all the requirements.

3.6.1 Steering Mechanism

In this section, the parametric equations are derived based on the locations of points O, A, B, C, P, and Q. The initial conditions are assumed in zero steering and zero camber angles and are selected to meet the requirements. These initial conditions represent the location of hard points; hence, they are refined during the entire design process to achieve the best results.

At first, all the lengths for the links are calculated as follows:

- Coupler length (AB):

$$L_1 = \sqrt{(x_{Ainitial} - x_{Binitial})^2 + (y_{Ainitial} - y_{Binitial})^2 + (z_{Ainitial} - z_{Binitial})^2} \quad (3\text{-}3)$$

- Mounting Points distance (OC):

$$L = \sqrt{(x_{Oinitial} - x_{Cinitial})^2 + (y_{Oinitial} - y_{Cinitial})^2 + (z_{Oinitial} - z_{Cinitial})^2} \quad (3\text{-}4)$$

- Crank length (OA):

$$r_1 = \sqrt{(x_{Oinitial} - x_{Ainitial})^2 + (y_{Oinitial} - y_{Ainitial})^2 + (z_{Oinitial} - z_{Ainitial})^2} \quad (3\text{-}5)$$

- Slider length (CB):

$$r_2 = \sqrt{(x_{Binitial} - x_{Cinitial})^2 + (y_{Binitial} - y_{Cinitial})^2 + (z_{Binitial} - z_{Cinitial})^2} \quad (3\text{-}6)$$

- Crank Tip to point P length (AP):

$$L_2 = \sqrt{(x_{Ainitial} - x_{Pinitial})^2 + (y_{Ainitial} - y_{Pinitial})^2 + (z_{Ainitial} - z_{Pinitial})^2} \quad (3\text{-}7)$$

- Slider Tip to point P length (BP):

$$L_3 = \sqrt{(x_{Binitial} - x_{Pinitial})^2 + (y_{Binitial} - y_{Pinitial})^2 + (z_{Binitial} - z_{Pinitial})^2} \quad (3\text{-}8)$$

- Camber coupler length (QP):

$$L_4 = \sqrt{(x_{Qinitial} - x_{Pinitial})^2 + (y_{Qinitial} - y_{Pinitial})^2 + (z_{Qinitial} - z_{Pinitial})^2} \quad (3\text{-}9)$$

Once these values are set, they can be used as constant values in geometric equations. A numerical approach was taken in this project to solve the geometry. First, the four-bar mechanism is solved to determine the locations of points A and B. Afterwards, using constant lengths of plate ABP and link PQ, location of point P can be determined at any moment during different steering angles.

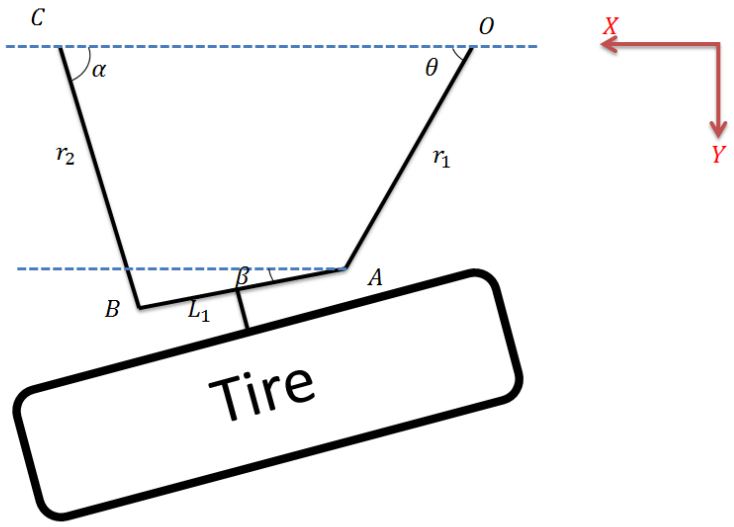

Figure 3-14: Defined parameters for the steering mechanism

At any instance, coordinates of points A and B can be found using the following equations.

$$x_A = x_O + r_1\cos(\theta) \tag{3-10}$$

$$y_A = y_O + r_1\sin(\theta)\,, \tag{3-11}$$

$$z_A = z_O \tag{3-12}$$

Similarly, for point B

$$x_B = x_C - r_2\cos(\alpha) \tag{3-13}$$

$$y_B = y_C + r_2\sin(\alpha) \tag{3-14}$$

$$z_B = z_O \tag{3-15}$$

Using the above equations, relationship between α and θ can be found using the fact that the distance between points A and B is fixed and equal to L_1.

$$L_1 = \sqrt{(x_A - x_B)^2 + (y_A - y_B)^2} \tag{3-16}$$

For any given θ, angle α and as a result locations of points A and B can be determined.

Moreover, having locations of points A and B at any instance can help to find the steering angle β using the following equation:

$$\beta = \text{atan}(\frac{y_B - y_A}{x_B - x_A}) \tag{3-17}$$

For the corner module designed in this project the final location of hard points are listed in Table 3-1.

Table 3-1: Coordinates of hard points for the steering mechanism

Coordinates\Points	O	A	B	C
x-coordinate (mm)	0	185	375	560
y-coordinate(mm)	0	200	200	0
z-coordinate(mm)	165	165	165	165

By changing angle θ steering angle β is calculated and graphed as illustrated in Figure 3-15.

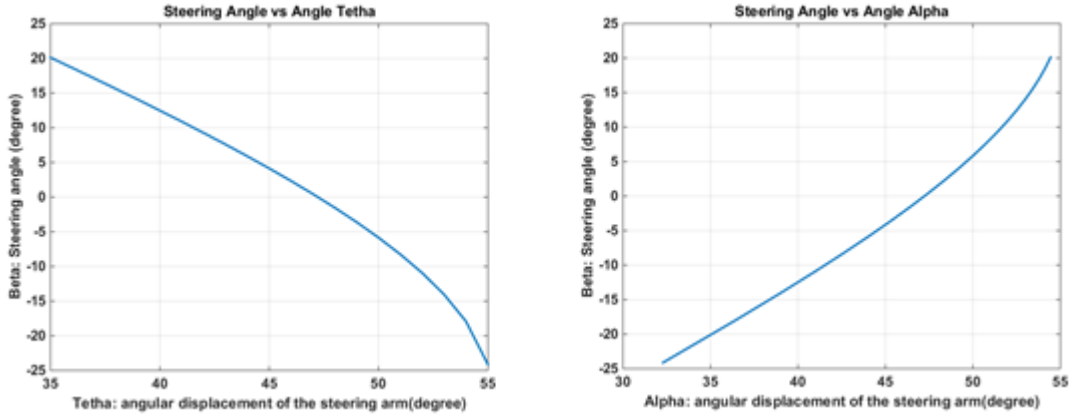

Figure 3-15: Steering angle change with respect to the angles of double rocker links

It can be seen that steering angle has a range from -20 degrees to 20 degrees which was required for the design. Another important observation is that the four-bar mechanism is far from its singular points at maximum steering angles. Singular point is where two of the links are aligned with each other. At the singular point, the direction of movement changes so suddenly and the behavior is highly nonlinear. As a result, it is very hard to precisely control the steering angle under large forces. It can also be observed from Figure 3-15 that as the steering angle gets closer to angle theta or angle alpha, the behavior becomes more nonlinear.

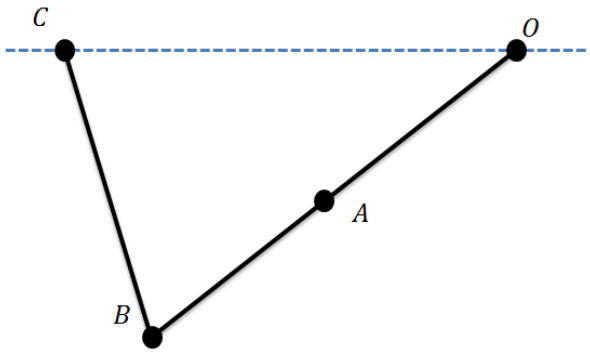

Figure 3-16: Singular point for a four-bar linkage; when links AB and AO are aligned.

Since the driver of the steering mechanism is a linear actuator, the behavior of steering angle should be studied against the actuator length. Once end points of the actuator are determined on link OA and the ground, the law of cosines can be employed to determine its length. For this project point F has coordinates of $(355.5,2.505,165)$ and point H_1 on link OA has coordinates of $(135.8,1468,165)$ when the steering angle is zero.

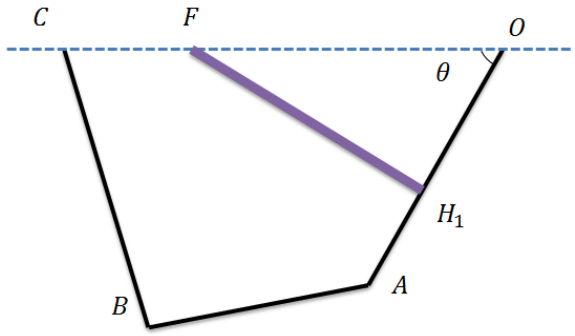

Figure 3-17: Four-bar mechanism OABC combined with actuator FH_1, where F is connected to the chassis and H_1 is connected to link AO.

At any given angle theta the actuator length can be calculated as follow:

$$FH_1{}^2 = OF^2 + OH_1{}^2 - 2 \times OF \times OH_1 \cos(\theta) \tag{3-18}$$

Figure 3-18 illustrates that for 6 centimeter change in actuator length, 40 degrees change in steering angle happens. It is noteworthy to mention that the hard points were defined so that the steering angle

changes almost linearly with any change in actuator length. This linear behavior is more significant when the steering angle is between -10 degrees to 10 degrees. This range is applied when the vehicle speed is high and the driver needs to have a linear feedback from steering system in order to control the vehicle best.

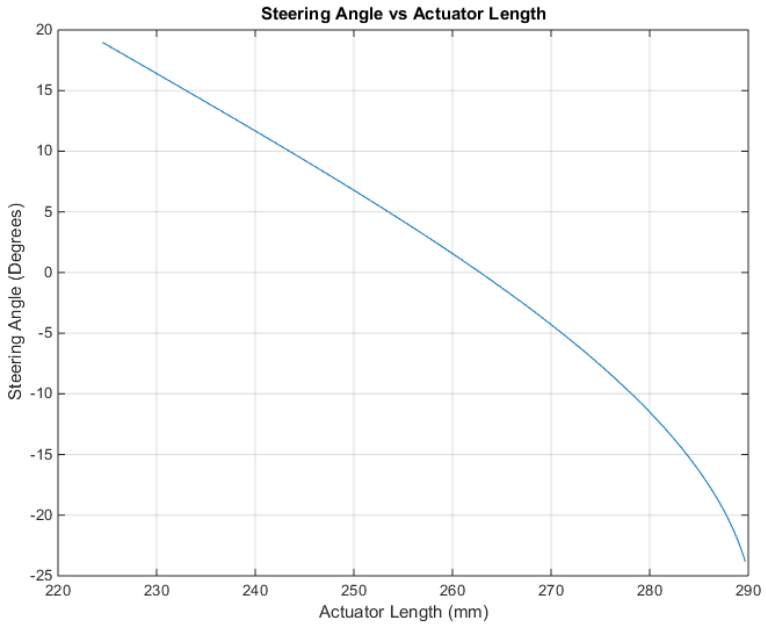

Figure 3-18: Steering actuator length vs steering angle

3.6.2 Camber Mechanism

The hard points for the camber mechanism were mainly picked to meet the packaging requirements while providing maximum 15 degrees of negative camber. The reason for -15 degrees requirement is discussed in chapter 4 and its effect on vehicle dynamic is studied in more details. The hard points for the camber mechanism are provided in Table 3-2.

Table 3-2: Locations of hard points for the camber mechanism

Coordinates\Points	Q	D	H2	E	P
x-coordinate(mm)	210	210	210	210	210
y-coordinate(mm)	93	0	96	0	200
z-coordinate(mm)	600	245	218	430	600

By contracting the length of actuator EH_2 the angle of AP changes with respect to Z axis as illustrated in Figure 3-19. Any deviation from the initial point denotes the camber angle of the wheel. In order to find the relationship between the actuator length and the camber angle "Adams/View" was used. The results are presented in Figure 3-20. It can be observed that the relationship between the camber angle and the actuator length is highly linear. Linear behavior greatly helps with controlling the camber. Furthermore, the driver receives a more clear feedback from the vehicle behavior and can control it better. It can also be seen from Figure 3-20 that camber angle changes 15 degrees by contracting the length of the actuator which was the design requirement for the camber mechanism.

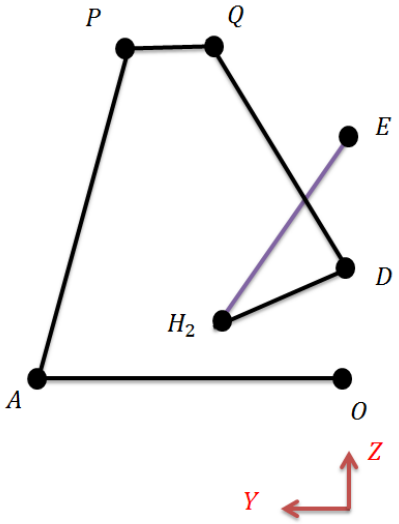

Figure 3-19: Side view of the camber mechanism. Any change in length of actuator EH_2 changes the angle of line AP with respect to Z axis. All the joints are revolute joints in this schematic.

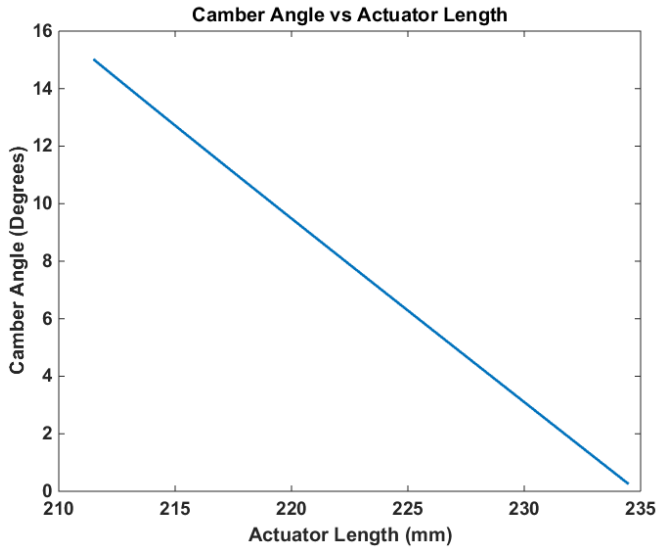

Figure 3-20: Camber actuator length demonstrates a linear relationship with camber angle.

In order to determine the required forces for the actuators the behavior of the kingpin axis is studied as discussed earlier. In full steering range from -20 degrees to 20 degrees, using MATLAB, the locus of tire's contact patch and the locus of the intersection of the kingpin axis and the ground is calculated and illustrated in Figure 3-21. The required actuator forces are presented later in chapter 5.

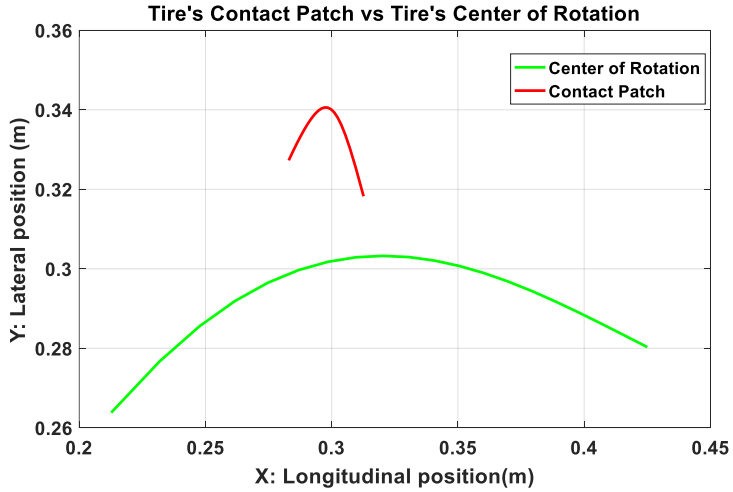

Figure 3-21: Locus of tire contact patch and intersection of the kingpin axis with ground during various steering angles.

It can be observed that as the tire moves to the right, the center of rotation moves to the left. Their distance is small at low steering angles which mainly happen at high speeds. As a result, at high speeds lower forces are exerted on the actuators and their response is faster.

Chapter 4
Effects of Corner Module on Vehicle Ride and Rollover

Urban vehicles mostly have narrow configurations which make them beneficial for relieving traffic congestion and shortage of parking spots. On the other hand, to meet passenger comfort and visibility requirements on the roads, these vehicles have to maintain the standard height required for road vehicles. Therefore, these vehicles have a relatively large height to width ratio. This characteristic reduces their rollover threshold which could be dangerous [26]. Rollover accidents cause nearly 30% of all deaths in car crashes [27]. As a consequence, it is mandatory to improve rollover threshold for these vehicles to make them safe. Previously, many researchers have worked on the various ideas to improve rollover threshold of narrow vehicles. Ideas such as differential braking systems [28] active steering [29] and active suspension systems [30] have been utilized to prevent rollover accidents. However, these methods affect yaw and lateral motions of the vehicle which is not favorable from the vehicle dynamic point of view. Moreover, ideas such as tilting mechanisms [31] have attained great achievements to prevent rollover; yet they are not favorable from the manufacturing point of view.

In this chapter, the camber control is considered to improve rollover threshold of narrow vehicles. In the camber control, increasing the camber angle increases wheel track and reduces height of the vehicle resulting in improved rollover threshold. In the corner module, an active camber is integrated in the design and its effect is studied in this chapter. The cambering has no effect on yaw motion of the vehicle as will be discussed later and is much cheaper than tilting mechanism for manufacturing purposes. Suspensions' spring stiffness has direct impact on performance of the cambering mechanism and rollover behavior of the vehicle. Hence, the spring stiffness should be calculated before studying the effect of camber on the rollover threshold.

4.1 Suspension Spring Stiffness

Ride quality is one of the most important functionalities of any suspension system. This quality is characterized based on the sensitivity of human body to vibration [32]. Appropriate spring stiffness results in high level of ride comfort. Stiffness of the springs can also greatly affect the rollover threshold and handling of the vehicle. In this section, the stiffness is determined based on ride quality and is improved iteratively to provide both ride comfort and rollover stability at the same time with higher priority given to ride comfort.

4.1.1 Quarter Car Model

To calculate stiffness of the springs for ride comfort, a 2-DOF quarter car model is used. This model considers a quarter of a car as a single wheel vehicle. Where m_s denotes the sprung mass and m_u is the un-sprung mass resulting in two degrees of freedom in vertical direction.

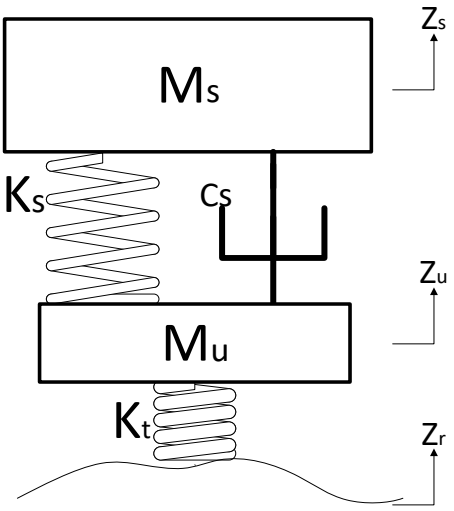

Figure 4-1: Quarter car model

Using the Newton's law, equations of motions for the quarter car model are as follows:

$$m_s\ddot{z}_s + c_s(\dot{z}_s - \dot{z}_u) + k_s(z_s - z_u) = 0 \quad (4\text{-}1)$$

$$m_u\ddot{z}_u + c_s(\dot{z}_u - \dot{z}_s) + k_s(z_u - z_s) + k_t(z_u - z_r) = 0 \quad (4\text{-}2)$$

In equations (4-1) and (4-2), K_t represents the stiffness of the tire, while K_s and C_s represent suspension stiffness and damping respectively. Moreover, Z_s, Z_u, and Z_r represent the vertical displacements of the sprung mass, un-sprung mass, and the road respectively.

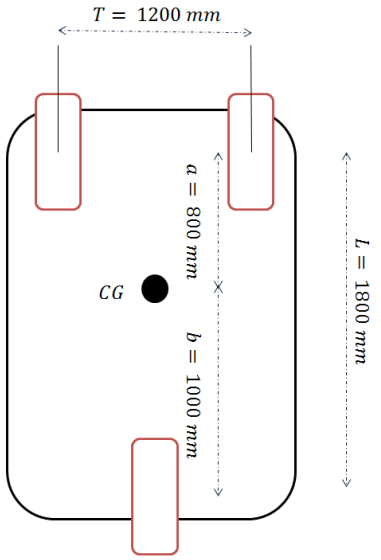

Figure 4-2: Three wheeled vehicle's dimensions and location of its center of mass.

And m_s for front and rear of the vehicle can be calculated based on "M", mass of the entire vehicle.

$Front$: $$m_s = \frac{b}{2L}M - m_u \tag{4-3}$$

$Rear$: $$m_s = \frac{a}{L}M - m_u \tag{4-4}$$

If we assume the road profile is sinusoidal in the form of $z_r = Z_r \sin(\omega t)$, then the solutions to differential equations (4-1) and (4-2) are in the form of:

$z_u = Z_u \sin(\omega t - \varphi_u)$ and $z_s = Z_s \sin(\omega t - \varphi_s)$

The following parameters are defined before calculating the appropriate spring stiffness for the three wheeled vehicle [33]:

- Natural frequency of the sprung mass is defined as $\omega_s = \sqrt{\frac{k_s}{m_s}}$ and the natural frequency of the un-sprung mass is defined as $\omega_u = \sqrt{\frac{k_t}{m_u}}$.
- Other parameters are defined as follows:

$\alpha = \frac{\omega_s}{\omega_u}$, $\varepsilon = \frac{m_s}{m_u}$, $\zeta = \frac{c_s}{2m_s\omega_s}$, and $r = \frac{\omega}{\omega_s}$

4.1.2 Transmissibility Ratio

Sprung mass transmissibility ratio is the ratio of the vibration amplitude of the sprung mass $Z_s$to that of the road profile Z_r. It can be proved that transmissibility ratio can be calculated using equation: [33]

$$\left|\frac{Z_s}{Z_r}\right| = \sqrt{\frac{4\zeta^2 r^2 + 1}{Z_1^2 + Z_2^2}} \tag{4-5}$$

where:

$$Z_1 = (r^2(r^2\alpha^2 - 1) + (1 - (1+\varepsilon)r^2\alpha^2)) \tag{4-6}$$

$$Z_2 = 2\zeta r(1 - (1+\varepsilon)r^2\alpha^2) \tag{4-7}$$

In general, for a quarter car model the frequency response for transmissibility ratio is similar to Figure 4-3. Where, there are two resonance peaks for two degrees of freedom of the quarter car model. The first peak is the resonance frequency of the sprung mass and the second peak is the resonance frequency of the un-sprung mass.

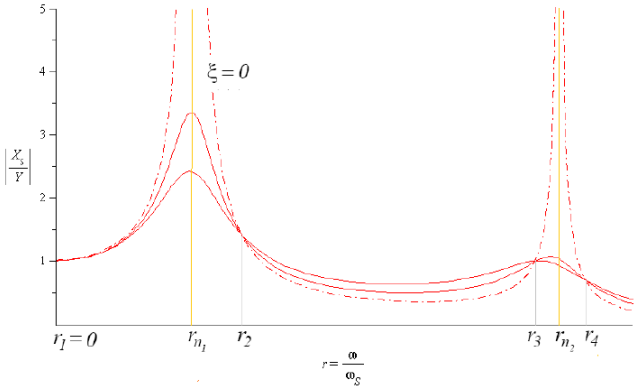

Figure 4-3: Typical frequency response of transmissibility ratio for quarter car models [34]

In Figure 4-3, r_{n1} and r_{n2} represent the resonance frequency ratios [33]:

$$r_{n1} = \sqrt{\frac{1}{2\alpha^2}(1 + (1+\varepsilon)\alpha^2 - \sqrt{(1 + (1+\varepsilon)\alpha^2)^2 - 4\alpha^2})} \tag{4-8}$$

$$r_{n2} = \sqrt{\frac{1}{2\alpha^2}(1 + (1+\varepsilon)\alpha^2 + \sqrt{(1+(1+\varepsilon)\alpha^2)^2 - 4\alpha^2})} \tag{4-9}$$

In order to find correct values of r_{n1} and r_{n2}, the sensitivity of human body to vibration must be taken into account. By looking at ride comfort criterion in Figure 4-4, it can be observed that between frequencies of 4 Hz to 8 Hz human body has the highest sensitivity to acceleration RMS and as a result the amplitude of vibration. Therefore, r_{n1} and r_{n2} must be selected in a way that minimum amplitude is provided for frequencies between 4 to 8 Hz. Therefore, these frequencies should lie on the anti-resonance zone of the transmissibility ratio graph. By many years of experiments, the two magic numbers for resonance peaks have been determined to be $f_{n1} = 1\ Hz$ and $f_{n2} = 10\ Hz$. And from these frequencies the values of r_{n1} and r_{n2} can be determined.

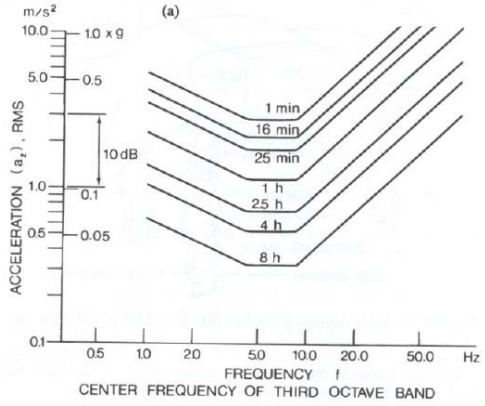

Figure 4-4: Evaluation of human exposure to whole-body vibration in vertical direction [32]

For this project same approach is undertaken and the spring stiffness is determined based of 1 Hz frequency for the sprung mass. Parameters in Table 4 1are used for the three wheeled vehicle in this project.

Table 4-1: Vehicle parameters

Vehicle Parameter	Value	Definition
M	750	Vehicle mass (kg)
a	0.8	Front wheel to CG distance (m)
b	1	Rear wheel to CG distance (m)
Ms	630	Sprung mass (m)

Calphaf	25000	Cornering stiffness for front tires
Calphar	40000	Cornering stiffness for rear tire
H	0.4	Vertical distance of CG
h	0.4	Vertical distance from RC to CG
T	1.2	Wheel initial track width (m)
Cs	1200	Spring damping coefficient
r	0.16	Ground clearance
l	1.8	Wheel base (m)

By solving equation (4-8) for $\omega_{n1} = 2\pi f_{n1} = 2\pi$ it can be seen that the stiffness for the spring is $k_s = 6828\ N/m$. This value results in the second frequency of 12.75 Hz which is acceptable for ride comfort. The effect of this value should be studied on roll behavior of the vehicle before finalizing this value for suspension stiffness.

4.2 Roll Dynamics

Another important effect of suspension spring stiffness is on the roll dynamics of the vehicle. The equations for roll can be written as [18]:

$$-m_s a_y h cos(\varphi) + m_s g h sin(\varphi) - k_t \varphi - c_t \dot{\varphi} = I_z \ddot{\varphi} \tag{4-10}$$

where the roll angle is φ, lateral acceleration is a_y, and k_t and $c_t$are tortional stiffness and torsional damping coefficient, respectively. I_z denotes the mass moment of inertia of the vehicle about the z axis. For small roll angles, the above equation can be linearized and rewritten as:

$$I_z \ddot{\varphi} + (k_t - m_s g h)\varphi + c_t \dot{\varphi} = -m_s a_y h \tag{4-11}$$

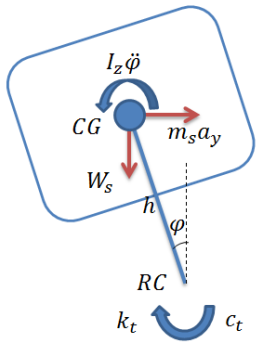

Figure 4-5: Free body diagram of vehicle rolling about its roll center with equivalent suspension roll stiffness and roll damping for equation (4-10)

In the steady state conditions when $\dot{\varphi} = \ddot{\varphi} = 0$, it can be seen that:

$$|\varphi_{ss}| = \frac{m_s a_y h}{k_t - m_s g h} \tag{4-12}$$

Using equation (4-12), the roll gain is defined as:

$$\frac{|\varphi_{ss}|}{a_y} = \frac{m_s h}{k_t - m_s g h} \tag{4-13}$$

In the above equations k_t and c_t are torsional stiffness and torsional damper installed at the roll center. These values can be determined based on spring stiffness and damping value of the suspension system. For small roll angles the assumption of vertical displacement $\Delta = \frac{\varphi T_s}{2}$ is valid [18] from Figure 4-6. Moreover,

$$M_t = F_s T_s \tag{4-14}$$

$$F_s = k_s \Delta = \frac{k_s \varphi T_s}{2} \tag{4-15}$$

As a result,

$$M_t = \frac{k_s T_s^2}{2} \varphi \tag{4-16}$$

$$k_t = \frac{M_t}{\varphi} = \frac{1}{2} T_s^2 k_s \tag{4-17}$$

It can be observed as k_s increases, k_t increases as well. In addition, increase in wheel track T_s results in increase of k_t as well.

Same approach can be used for calculation of torsional damping which results in:

$$c_t = \frac{1}{2} T_s^2 c_s \tag{4-18}$$

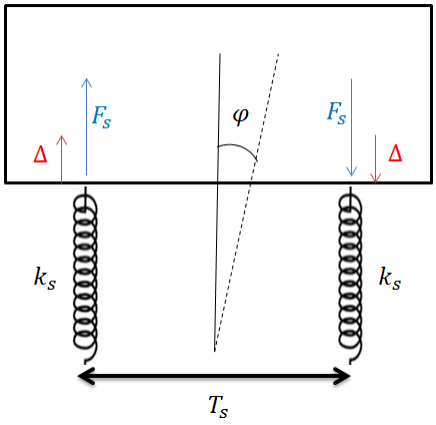

Figure 4-6: Diagram for calculating suspension roll stiffness

For the three wheeled vehicle, torsional spring for the front and rear axles can be calculated as:

- Front torsional stiffness: $$k_{tf} = \frac{1}{2} \times (1.2)^2 \times k_{sf} \tag{4-19}$$
- Rear torsional stiffenss: $$k_{tr} = \frac{1}{2} \times (0)^2 \times k_{sr} \tag{4-20}$$
- Total torsional stiffness: $$k_t = k_{tf} + k_{tr} \tag{4-21}$$

Using the spring stiffness found in Section 4.1.2, it can be seen that the roll gain is 58 degrees/ g. This value is very high and indicates poor roll dynamics of the vehicle. Roll gain can be reduced by increasing the spring stiffness and sacrificing the ride comfort. For the second iteration, the sprung mass natural frequency is increased to be 1.3 Hz. This value still provides an acceptable ride comfort for shorter travels. Using this value, spring stiffness is calculated to be 11765 N/m. This spring stiffness results in a roll gain with the value of 23 degrees/g. It can be seen that this value is improved by about 50 percent. However, it still does not provide an acceptable roll dynamic for the vehicle and further improvement is necessary.

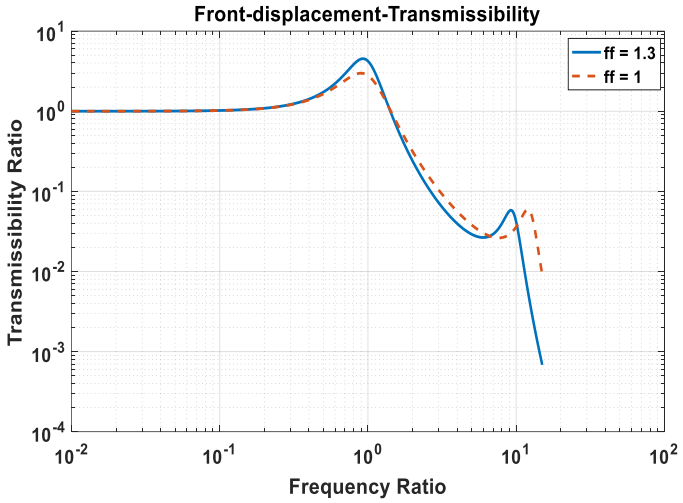

Figure 4-7: Transmissibility ratio for 1 Hz vs 1.3 Hz for the first natural frequency of the vehicle. It can be seen the natural frequency of 1 Hz with softer spring provides a smoother response with lower resonance peaks.

In general, to improve roll gain of conventional vehicles, an anti-roll bar is installed. Anti-roll bar acts as a torsional spring and demonstrates stiffness only when the left and right wheels are moving out of phase. Otherwise, this bar does not show any stiffness and as a result does not affect the ride dynamic of the car. However, installing an anti-roll bar contradicts with the idea of having an independent corner module. Hence, camber mechanism is utilized instead to further improve roll dynamics without sacrificing ride comfort.

4.3 Effect of camber on vehicle geometry

In general, wheels camber causes deformation in tires which creates lateral forces on tires. These forces affect lateral and yaw motion of the vehicle. In some cases such as in motor cycles camber forces are used for steering purposes as well.

In this project, only equal negative camber angles are applied to both front wheels. Therefore, tire forces generated by camber are equal and in opposite direction, which result in no effect on lateral and yaw behavior of the vehicle. Nevertheless, this cambering action can change the geometry of the vehicle as necessary and improve the rollover threshold of the vehicle.

This action has three main impacts on the geometry of the vehicle. Firstly, it increases the wheel track which improves the torsional stiffness of the vehicle as discussed in section 4.2. Secondly, the center of mass of the vehicle drops and gets closer to the ground. Finally, the vertical stiffness of the springs is increased. All the above mentioned features improve the rollover threshold of the vehicle.

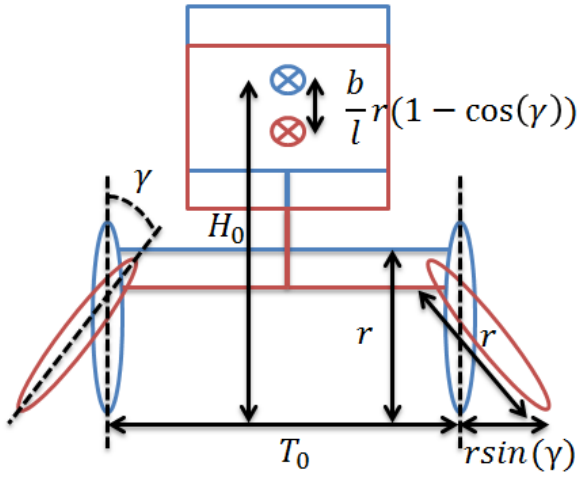

Figure 4-8: Effect of camber on geometry of the vehicle

If each wheel is cambered by γ degrees, the front track is increased as depicted in Figure 4-8 by:

$$T = T_0 + 2rsin(\gamma) \tag{4-22}$$

Moreover, the center of mass of the vehicle is lowered by $\frac{b}{l}r(1-\cos(\gamma).\frac{b}{l}$ that comes from the fact that camber is only applied to the front axle, hence the elevation of rear axle does not change.

$$H = H_0 - \frac{b}{l}r(1-\cos(\gamma)) \tag{4-23}$$

By changing the angle of suspension, for the same road input, spring contraction is different. As a result, by writing energy equations, the equivalent spring stiffness of angled suspension can be calculated from:

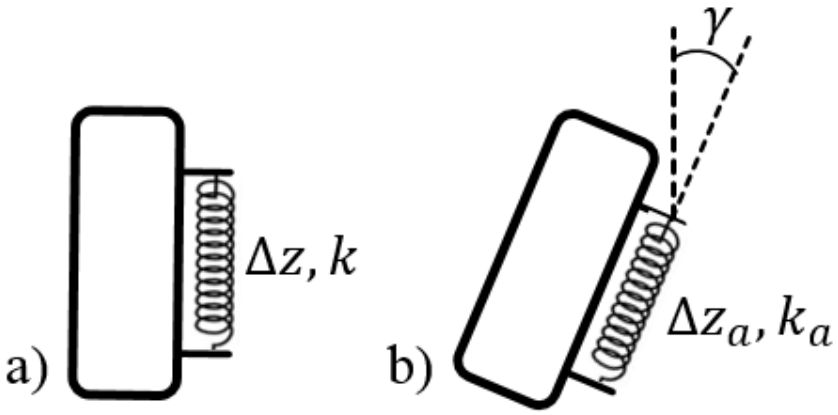

Figure 4-9: a) Equivalent suspension travel and spring stiffness. b) Actual suspension travel and spring stiffness for the same road input.

$$\Delta z_a = \frac{\Delta z}{cos(\gamma)} \tag{4-24}$$

$$E_a = E_b \rightarrow \frac{1}{2} k \Delta z^2 = \frac{1}{2} k_a \Delta z_a^2 \rightarrow k = \frac{k_a}{cos^2(\gamma)} \tag{4-25}$$

Since, $\cos(\gamma)$ is always less or equal to 1, equivalent stiffness k is always greater than k_a.

4.4 Roll-over Analysis

In this section, the roll-over behavior of the three wheeled vehicle with the proposed corner module is studied in dynamic conditions. A three degree of freedom model is used for modeling the vehicle. Two degrees of freedom are derived from the linear bicycle handling model and one degree of freedom is derived from the roll equation. For the bicycle handling model, the linearized equations are derived as follows:

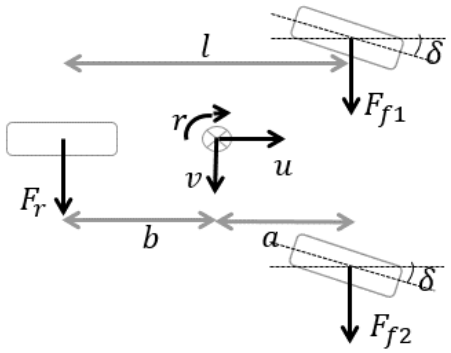

Figure 4-10: Top view of three wheeled vehicle with longitudinal and lateral velocity and yaw rate for the linear bicycle model.

$$F_{f1} + F_{f2} + F_r = M(\dot{v} + ur) \tag{4-26}$$

$$a(F_{f1} + F_{f2}) - b(F_r) = I_z\dot{r} \tag{4-27}$$

The roll equation as the third degree of freedom is written as follows for small roll angles:

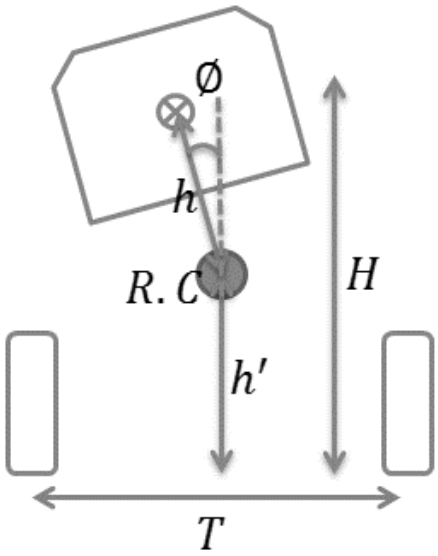

Figure 4-11: Front view of the vehicle during rolling about it roll center

$$I_x\ddot{\emptyset} + c_t\dot{\emptyset} + (k_t - m_s gh)\emptyset = -m_s h(\dot{v} + ur) \tag{4-28}$$

In equations (4-26) and (4-27), tire forces are assumed to be linear. Ergo, tire forces can be written as follows [18]:

$$F_{f1} = c_{\alpha f}\alpha_f + c_\gamma \gamma \tag{4-29}$$

$$F_{f2} = c_{\alpha f}\alpha_f + c_\gamma(-\gamma) \tag{4-30}$$

$$F_r = c_{\alpha r}\alpha_r \tag{4-31}$$

From equations (4-29) and (4-30) it can be observed that tire forces due to camber cancel each other out as long as the camber angles are the same in opposite directions. As a result, symmetric negative cambering does not affect the lateral and yaw behavior of the vehicle. It must be mentioned that this conclusion is only correct when the camber coefficient c_γ is constant. In general this parameter is a function of normal force on the tire. During cornering and maneuvers the normal loads on tires is different due to lateral load transfer; therefore, camber coefficient is different for left and right tires. However, in this thesis this effect is assumed minimal and the camber coefficient is considered constant. Moreover, sideslip angles for both front and rear tires in the linear zone can be determined as:

$$\alpha_f = \delta + \left(\frac{v + ar}{u}\right) \tag{4-32}$$

$$\alpha_r = -\left(\frac{v - br}{u}\right) \tag{4-33}$$

By replacing equations (4-32) and (4-33) into equations (4-26), (4-27), and (4-28), the following equations can be obtained:

$$\dot{v} = \frac{2c_{\alpha f}}{M}\delta + \frac{-2c_{\alpha f} - c_{\alpha r}}{uM}v + \left(\frac{-2ac_{\alpha f} + bc_{\alpha r}}{um} - u\right)r \tag{4-34}$$

$$\dot{r} = \frac{2ac_{\alpha f}}{I_z}\delta + \left(\frac{-2ac_{\alpha f} + bc_{\alpha r}}{uI_z}\right)v + \frac{-2a^2c_{\alpha f} - b^2c_{\alpha r}}{uI_z}r \tag{4-35}$$

$$\ddot{\emptyset} = \frac{-m_s h}{I_x}\left(\frac{2c_{\alpha f}}{M}\right)\delta + \frac{m_s h}{I_x}\left(\frac{2c_{\alpha f} + c_{\alpha r}}{uM}\right)v - \frac{m_s h}{I_x}\left(\frac{-2ac_{\alpha f} + bc_{\alpha r}}{uM}\right)r - \frac{c_t}{I_x}\dot{\emptyset} + \frac{m_s gh - k_t}{I_x}\emptyset \tag{4-36}$$

These equations can be used for the state space form of the vehicle model. The state space equations in matrix form have the form of $\dot{X} = AX + B\delta$ with $X^T = [v \quad r \quad \emptyset \quad \dot{\emptyset}]$. A and B matrices are:

$$A = \begin{bmatrix} \frac{-2c_{\alpha f} - c_{\alpha r}}{uM} & \left(\frac{-2ac_{\alpha f} + bc_{\alpha r}}{um} - u\right) & 0 & 0 \\ \left(\frac{-2ac_{\alpha f} + bc_{\alpha r}}{uI_z}\right) & \frac{-2a^2c_{\alpha f} - b^2c_{\alpha r}}{uI_z} & 0 & 0 \\ 0 & 0 & 0 & 1 \\ \frac{m_s h}{I_x}\left(\frac{2c_{\alpha f} + c_{\alpha r}}{uM}\right) & \frac{m_s h}{I_x}\left(\frac{-2ac_{\alpha f} + bc_{\alpha r}}{uM}\right) & \frac{m_s gh - k_t}{I_x} & -\frac{c_t}{I_x} \end{bmatrix}$$

$$B = \begin{bmatrix} \frac{2c_{\alpha f}}{M} \\ \frac{2ac_{\alpha f}}{I_z} \\ 0 \\ \frac{-m_s h}{I_x}\left(\frac{2c_{\alpha f}}{M}\right) \end{bmatrix}$$

4.5 Roll-over Index

In the previous section, roll-gain was used to determine the rollover performance of the vehicle. However, roll-gain is only for steady state conditions and is not a proper measure in dynamic analysis. In this section roll-over index is introduced as the performance measure [35].

Rollover threshold is defined as the state of the vehicle when normal forces on one of the tires are zero due to lateral load transfer. Furthermore, the rollover index is defined as [36]:

$$RI = \frac{F_l - F_r}{F_l + F_r} \tag{4-37}$$

Using the above equation, it is evident that as long as $-1 < RI < 1$ the vehicle never reaches its rollover threshold and both tires are in contact with the road. Because the front and rear tire forces are not directly measureable, equation (4-37) is rewritten in terms of measurable parameters such as lateral acceleration and roll angle.

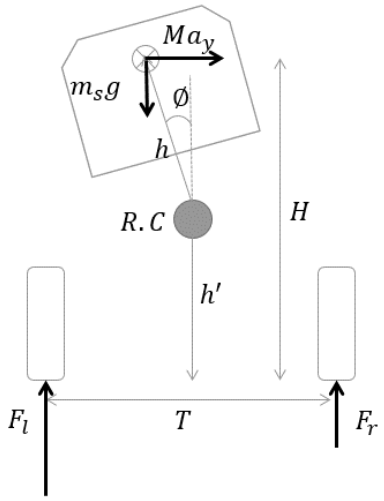

Figure 4-12: Front view of the vehicle. During lateral load transfer normal forces on the tires differ.

Moment equation about roll center can be written as:

$$(F_l - F_r)\frac{T}{2} = -Ma_y h\cos(\emptyset) + m_s g h\sin(\emptyset) \tag{4-38}$$

and vertical force equation can be written as:

$$(F_l + F_r) = \frac{b}{l}Mg \tag{4-39}$$

By replacing equations (4-38) and (4-39) into rollover index equation (4-37), rollover index can be rewritten in the form of:

$$RI = \frac{-2a_y h\cos(\emptyset) + 2\frac{m_s}{M} g h\sin(\emptyset)}{\frac{b}{l}Tg} \tag{4-40}$$

In order to evaluate the rollover behavior of the vehicle, the vehicle model was built in Simulink and it was run for a standard double lane change maneuver as illustrated in Figure 4-13. The output of the model is rollover index and as long as $-1 < RI < 1$ the vehicle is stable. The inputs to the model are front steering angle, and vehicle speed which is set to be 35 km/h for this maneuver.

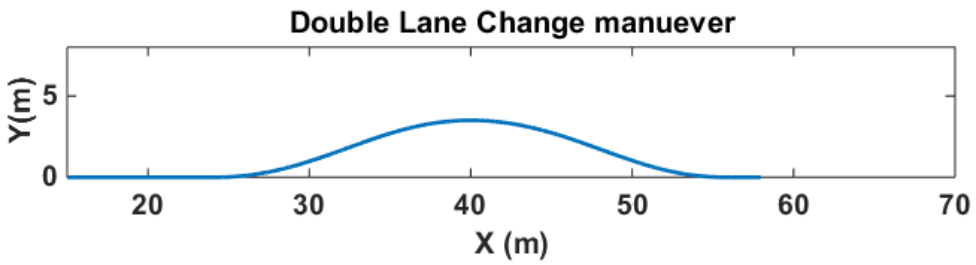

Figure 4-13: Double lane change maneuver.

To ensure the vehicle can follow the path accurately, a driver model was used to generate steering input for the vehicle. The driver model is a simple lead-lag controller and its gains were tuned by trial and error. From Figure 4-16 it can be observed that this driver can follow the path closely.

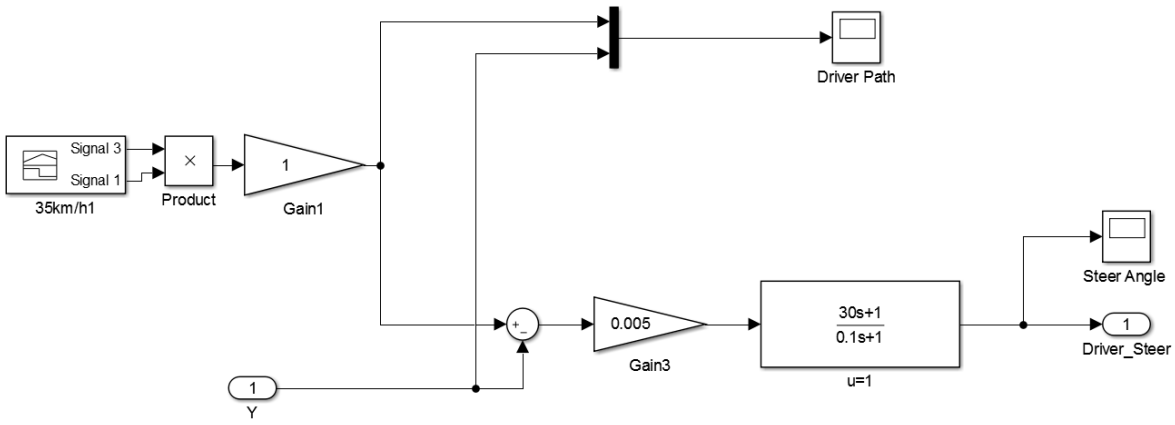

Figure 4-14: Lead-lag controller to model the driver in Simulink.

This driver generates steering input as illustrated in Figure 4-15.

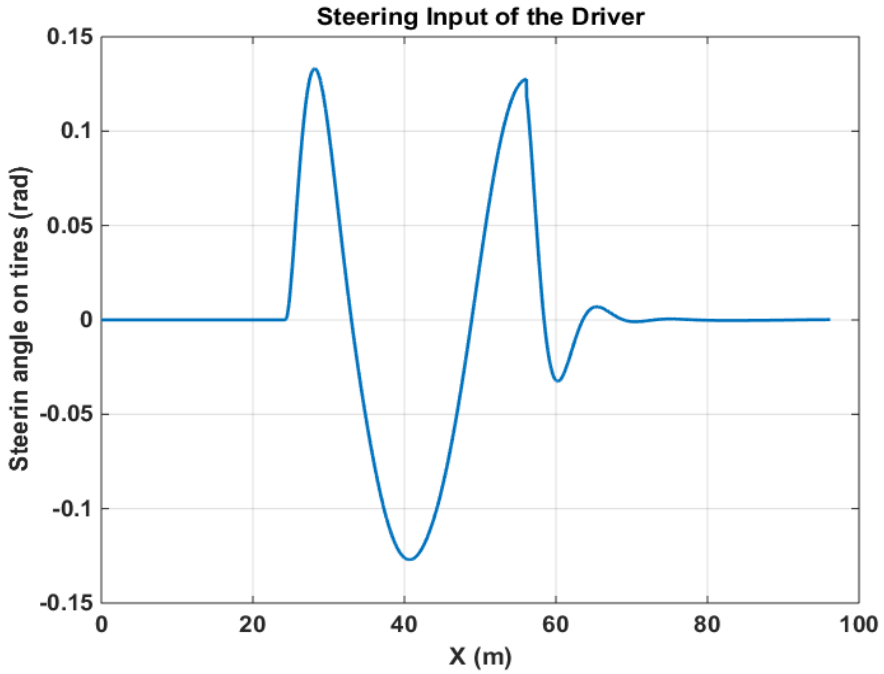

Figure 4-15: Steering input of the driver during double lane change.

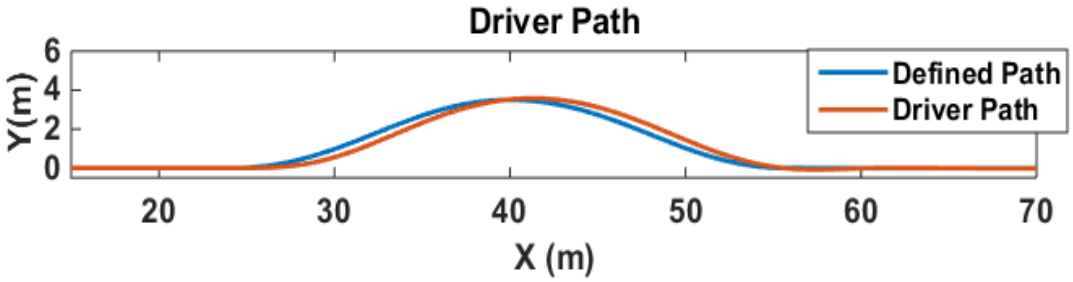

Figure 4-16: The driver follows the predefined path closely.

The first assumption was the linear model of the tires. To ensure this assumption is valid, the side slip of the tires are calculated and shown in Figure 4-17.

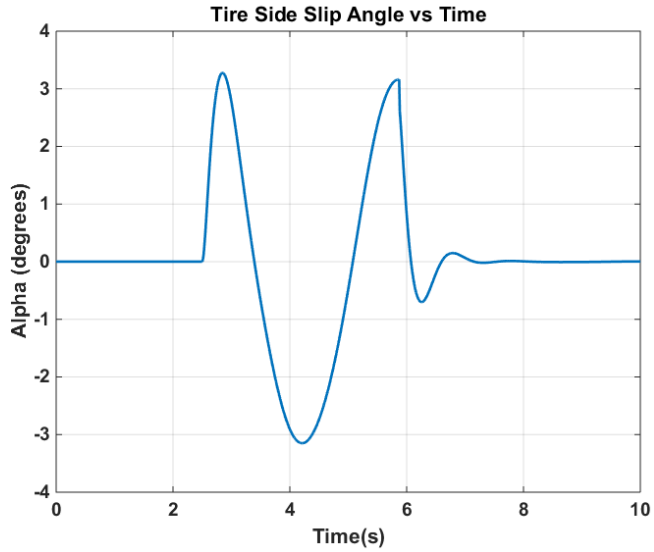

Figure 4-17: Tire side slip angle is less the 4 degrees, which indicates the tire is in its linear zone.

It can be observed form Figure 4-17 that the tire side slip angle is always less than 4 degrees which lies in the linear zone of the tire curve. As a result, the linear tire assumption is valid for this maneuver and the results are reliable.

As it is depicted in Figure 4-18 it can be seen that by applying maximum camber, -15 degrees, the rollover index decreases by almost 13%.

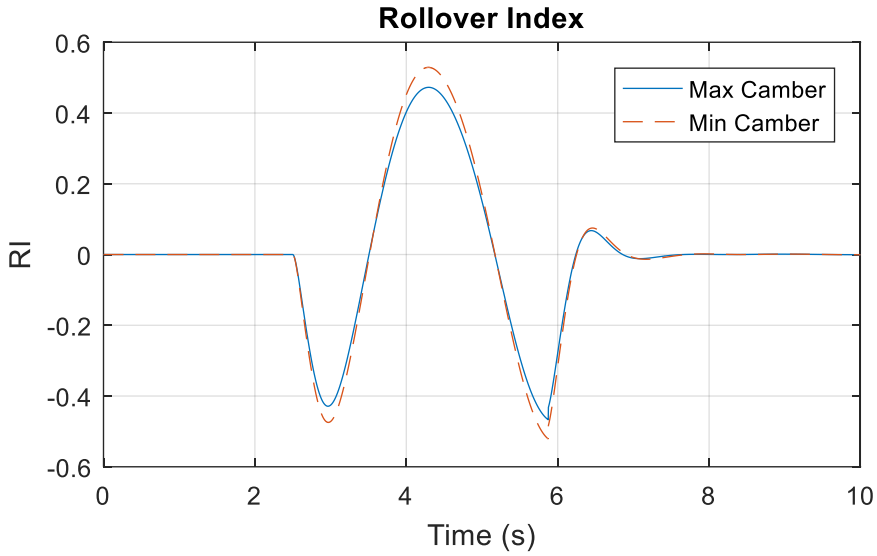

Figure 4-18: Rollover index during double lane change with no camber and maximum camber of the wheels.

This shows that cambering mechanism can be used as necessary to improve the rollover threshold of the vehicle. Moreover, roll angle decreases as well. In Figure 4-19 it is illustrated that roll angle is reduced by applying negative camber angle. This proves that roll stiffness of the vehicle is increased and roll gain is improved as well.

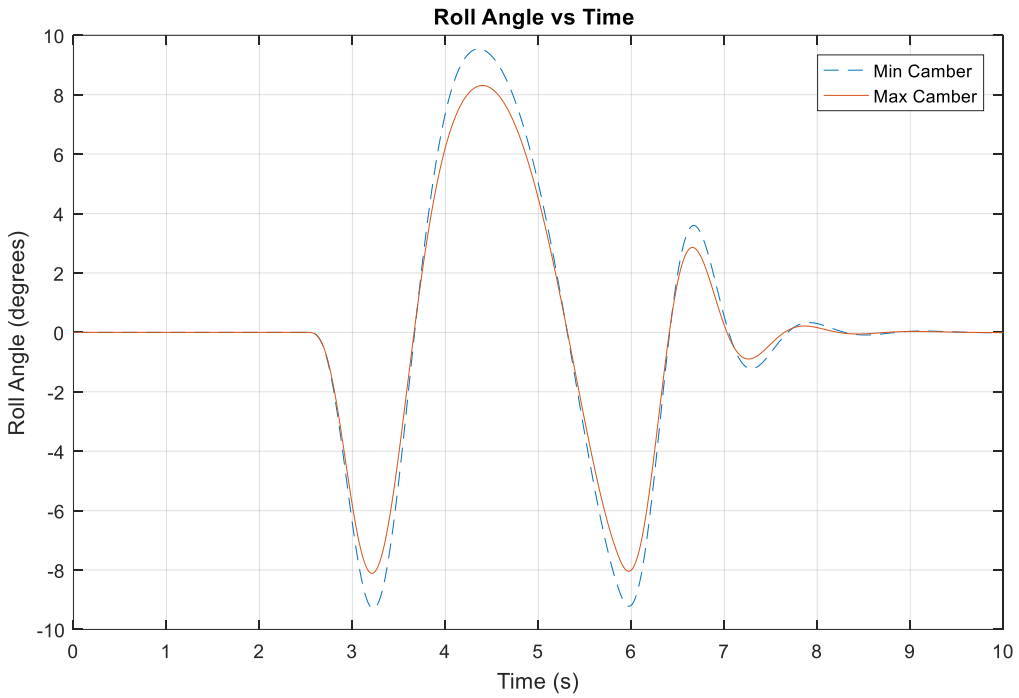

Figure 4-19: Roll angle during the double lane change maneuver with no camber and maximum camber of the wheels.

Based on the rollover study in this section it can be concluded that utilizing the camber mechanism can improve the rollover threshold specifically for narrow vehicles. Therefore, the next step should be the design of the corner module in a feasible manner.

Chapter 5
Detailed Design of Corner Module

In this section, the embodiment and detailed design of the concept is studied. The components of the corner module are selected from a wide range of off-shelf products that are available in market. In addition, all the links for the mechanisms are designed to meet packaging and load requirements of the corner module.

In order to find the loads an ADAMS/View model was created. Adams is commercial software for multi-body dynamics. In this model all the links are assumed as rigid links. Thereafter, boundary conditions and external loads are applied on the system to determine forces and torques exerted on each joint. By having an understanding of the amount of loads on the joints of each link, an educated guess can be made on the shape of the links in the initial stage. Later, these shapes are improved and refined based on kinematics and finite element analysis on the structure. In finite element analysis, the structure is analyzed based on the amount of the stress generated within the body. The shapes and materials are determined so that the maximum amount of the stress in a body is always less than its yield stress. Furthermore, a factor of safety of two is considered for this design. Keeping the material in its elastic zone, below its yield stress, ensures no permanent deformation and increased life time in the chassis system. This approach to the design is an iterative process in which the links are designed to meet packaging requirements, and then finite element analysis is performed on the structure for further improvements. Thereafter, the process starts over again and all the changes are applied to ADAMS model and solid model. This iterative process continues until the optimum structure is achieved. In the next sections only the final version is discussed.

5.1 ADAMS/VIEW Model

Based on the hard points determined from kinematic analysis, a model was created in ADAMS/view. This model consists of two arms with revolute joints connected to the body which serves as the steering mechanism combined with a linear actuator. The camber mechanism is also connected to the body through revolute joints. However, the floating link that connects the camber mechanism to the top of the spindle has two ball joints. This ensures the wheel has all the required degrees of freedom.

Moreover the suspension system is constrained in a plane by a vertical slider mechanism. This planar mechanism consists of four vertical rods and a floating spindle that can move freely in the vertical direction and there are spring and damper located on top of it to perform as the suspension system. Four

rods are placed in a rectangular pattern to ensure relatively high torsional rigidity of the structure. Otherwise, the steering mechanism demonstrates high compliance which is not desirable. The vertical suspension was selected to meet packaging requirements as well as satisfying high camber angle requirements of the corner module.

In this model, the external loads were applied on the contact patch of the tire from the road. And the connections to the body were assumed fixed. The extreme loading cases were applied in three different directions. 5g load in vertical direction, 2g load in longitudinal direction, and 2g load in lateral direction were applied on the corner module separately. 5g acceleration is chosen to simulate the forces exerted on the chassis system when the vehicle hits a bump at high speeds. In general, 1g longitudinal is the maximum acceleration exerted on the vehicle which happens during emergency braking. However, 2g accelerations are chosen for the design to withstand low speed impacts such as hitting curbs during parking of the vehicle as well. Similarly 1g lateral acceleration is the maximum acceleration applied to the vehicle before the vehicle starts sliding sideways or reaches its rollover threshold. Nevertheless, the main reason to apply such high loads is to find actuators that can handle high loads, so that are very fast under lower loads. Since all the g loads are exerted on the full vehicle the equivalent force on each wheel had to be determined for this analysis. These loads were applied statically in different configurations for steering and camber to find the worst case scenario. It turned out that 2g of lateral load in maximum steering and maximum camber exerts the largest forces on the links and the joints of the corner module as depicted in Table 5-1. These loads on the joints provide enough data for initial phase of the design. The FEA is performed on the system in its worst case from Adams' simulations. However, the amount of loads are less for the FEA and are closer to real loads applied on test vehicles from flat roads. These loads are reduced to 1g lateral combined with 1g vertical for FEA in this project.

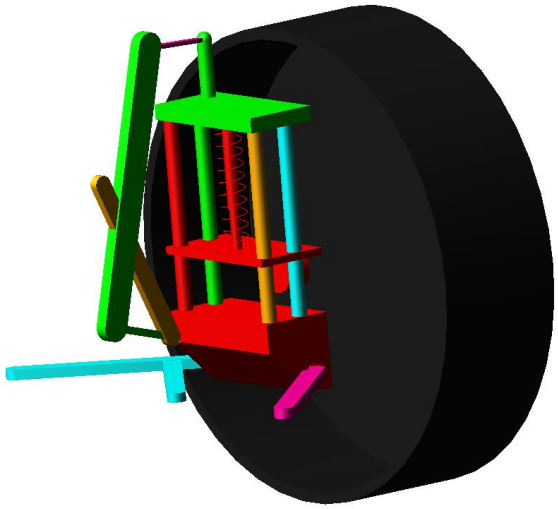

Figure 5-1: Corner module model in ADAMS/View

Table 5-1: Loads on the joints under 2g lateral acceleration

2g Lateral (6104 N)	Force-X (N)	Force-Y (N)	Force-Z (N)	Torque-X(N.m)	Torque-Y(N.m)	Torque-Z(N.m)
Crank	-5487	-5613	-9457	-1932	2760	0
Coupler A	-35380	-24770	-11910	0	0	0
Coupler B	-33560	-14770	-7030	0	0	0
Slider	3667	-4382	4577	1525	0	0
Floating Link	1820	3891	1829	0	0	0
Steering Actuator	29900	19160	2454	0	0	0
Camber Actuator	1820	2071	3285	247	0	0

5.2 Detailed Design

Based on the load analysis and selection of the components the corner module was manifested into its final version as illustrated in Figure 5-2. All the components are design so that all the packaging requirements are met.

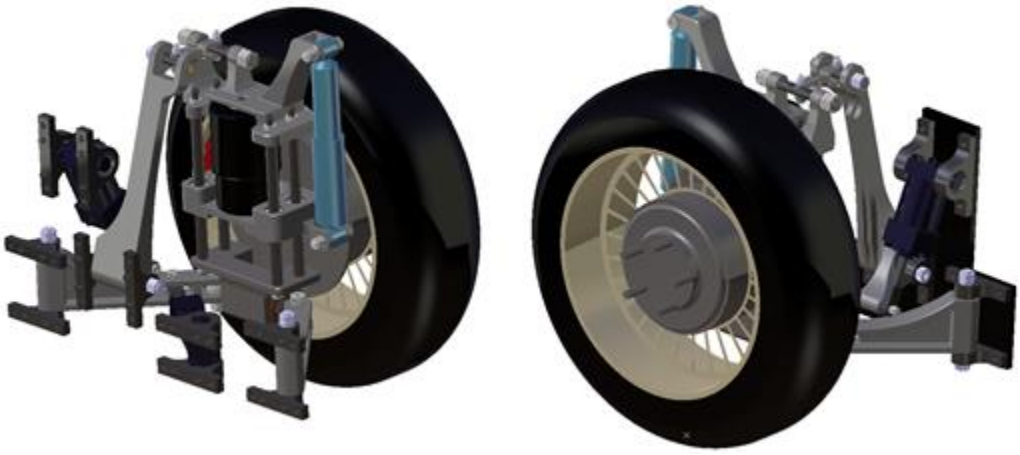

Figure 5-2: Final design of the corner module.

The four bar mechanism is placed at the bottom and can provide steering angles between -20 to +20 degrees with minor wheel travel. It ensures the mechanism can meet the design requirements. However, it can be observed from Figure 5-4 that steering alone results in minor camber of the wheel. Therefore, active cambering must be in place to compensate for this behavior and optimize the handling of the vehicle.

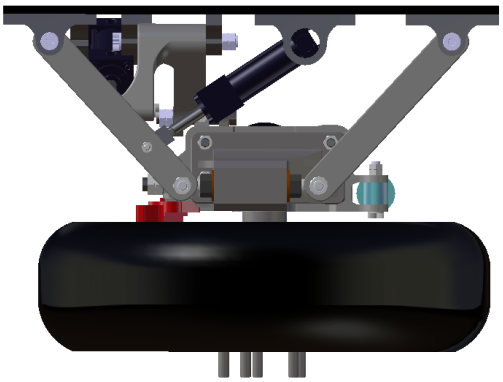

Figure 5-3: Bottom view of the corner module with zero steering angle.

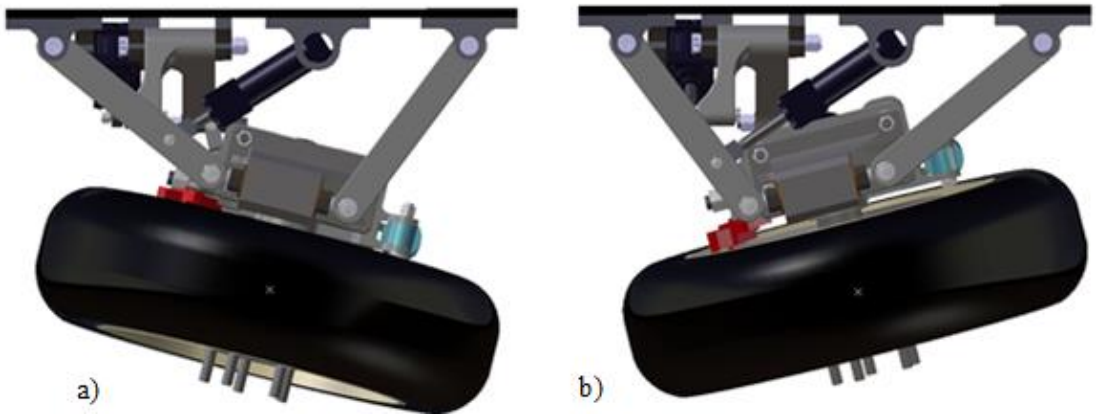

Figure 5-4: a) bottom view of the corner module with 15 degrees of steering angle. b) Bottom view of the corner module with -15 degrees of steering angle. It can be seen the contact patch of the wheel has negligible travel due to steering.

The steering actuator was selected to meet the load requirements calculated from the ADAMS simulations. This actuator can also provide more than 7 centimeter of stroke which is required to provide full steering for the corner module.

Moreover, it can be seen that the arms of the four-bar mechanism in Figure 5-5 are thicker and stronger at their connection point to the body of the vehicle. This is to make sure these arms can handle all the bending loads on this end. The validity of this design is confirmed by finite element analysis at the end of this chapter.

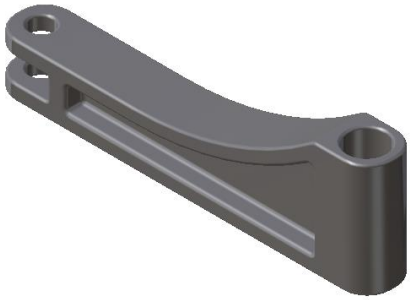

Figure 5-5: Four-bar mechanism arms.

The coupler of the four-bar in Figure 5-6 is designed in a way that only allows the bottom spindle to rotate about it. The lateral movement of the spindle is restricted by placing trust washer at its both ends. In addition, placing bronze bushings between the coupler and the bottom spindle allows its smooth rotation about the coupler. The bushing is press fitted inside the bottom spindle.

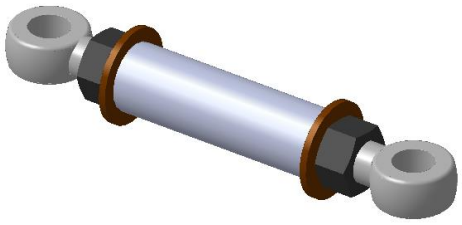

Figure 5-6: Four-bar mechanism coupler. Two trust washers at the end restrict the motion of the bottom spindle in lateral directions while it is free to rotate about the coupler.

The combination of the two arms, actuator, and coupler creates a four-bar mechanism that provides one degree of freedom for steering purposes. Furthermore, it allows rotation of the spindle about its coupler which is required to meet camber requirements.

The first packaging requirement was to fit all the mechanisms within 30 cm of the wheel. It can be seen from Figure 5-7 that the design meets this requirement. All the mechanisms, components, and the back plate are fitted within the predefined space.

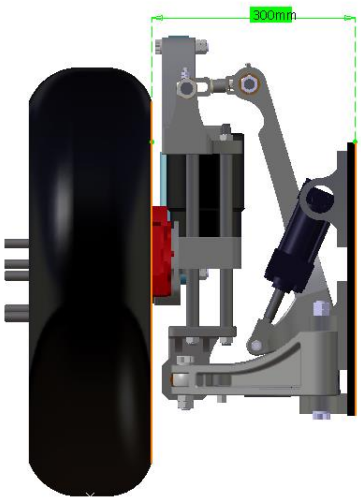

Figure 5-7: Side view of the corner module. All the mechanisms are packages within 30 centimeter of the wheel as required.

Moreover, the camber mechanism has to provide 15 degrees of negative camber. The kinematic shows that this requirement is also met by this design as illustrated in Figure 5-8. The camber actuator is also selected based on load calculations in ADAMS. This actuator provides enough stroke length for this application as well.

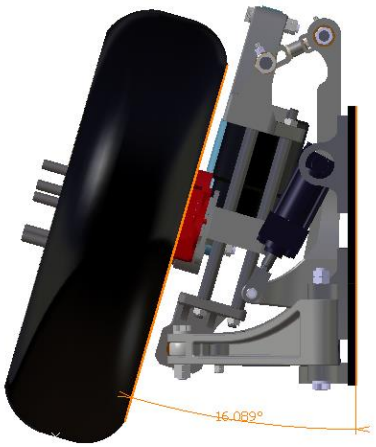

Figure 5-8: Side view of the corner module with maximum camber at zero steering.

The floating link that connects the camber mechanism to the top spindle has to be connected by ball joints on both ends to provide all the degrees of freedom for the corner module. However, most of the ball joints available in market that can handle high loads, do not meet the swivel angle requirements for this application. As a result, this part was designed from scratch to overcome this problem. As it can be observed in Figure 5-9 there are two pins connected to the camber link and the top spindle which can rotate freely about their axes. Moreover, the floating link consists of two clevises that can rotate about the mentioned pins at two ends. And finally, the two clevises can also rotate relative to each other about their axis of connection. This configuration performs similar to having two ball-joints at the ends; therefore it ensures all the degrees of freedom are met and the mechanism does not lock up. Bushings are placed between each two connection to make sure these joints can operate smoothly with an acceptable life cycle.

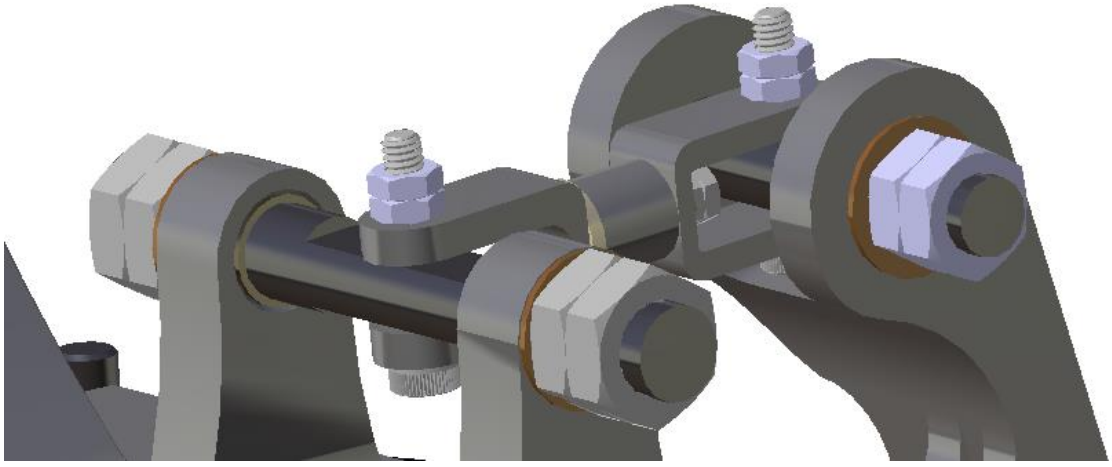

Figure 5-9: Floating link that connects the top spindle to the camber link. This link provides required degrees of freedom for the module to satisfy steering and camber requirements.

ADAMS calculations show that the amount of bending load on the camber link in Figure 5-10 is high. As a result, two ribs are added to this link to provide higher stiffness and strength. The shape is defined in a way that no internal collision with other components occurs during high steering and high camber angles.

Figure 5-10: Camber link. Two ribs along the length of the link increase its bending stiffness.

The suspension system is comprised of an air spring and a damper. The air spring was chosen as opposed to coil spring mainly because it is more compact and it can also keep the natural frequency of the vehicle constant under variable loads. The air spring sits on the floating spindle and only acts in vertical direction. All the lateral forces and torques are taken by the four rods that constraint the motion only in the vertical direction. Moreover, the damper is installed on the side and only acts in the vertical direction as well. This configuration is chosen to meet the packaging requirement for a highly compact design as shown in Figure 5-11. The air spring and the damper are selected in a way that provide the required stiffness and damping for the system. Furthermore, this suspension mechanism provides 7.5 cm of vertical wheel travel in each direction from its nominal point.

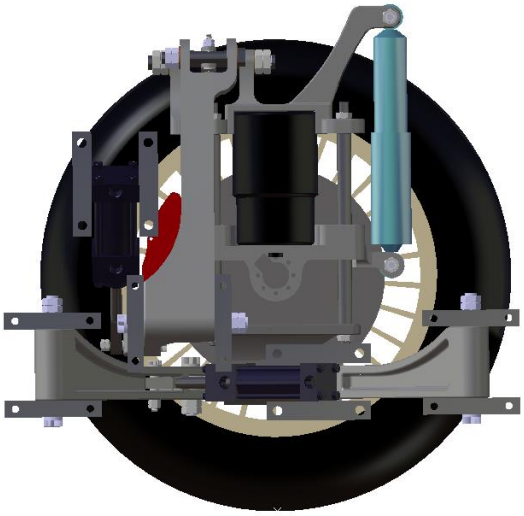

Figure 5-11: Back view of the corner module at its nominal suspension position.

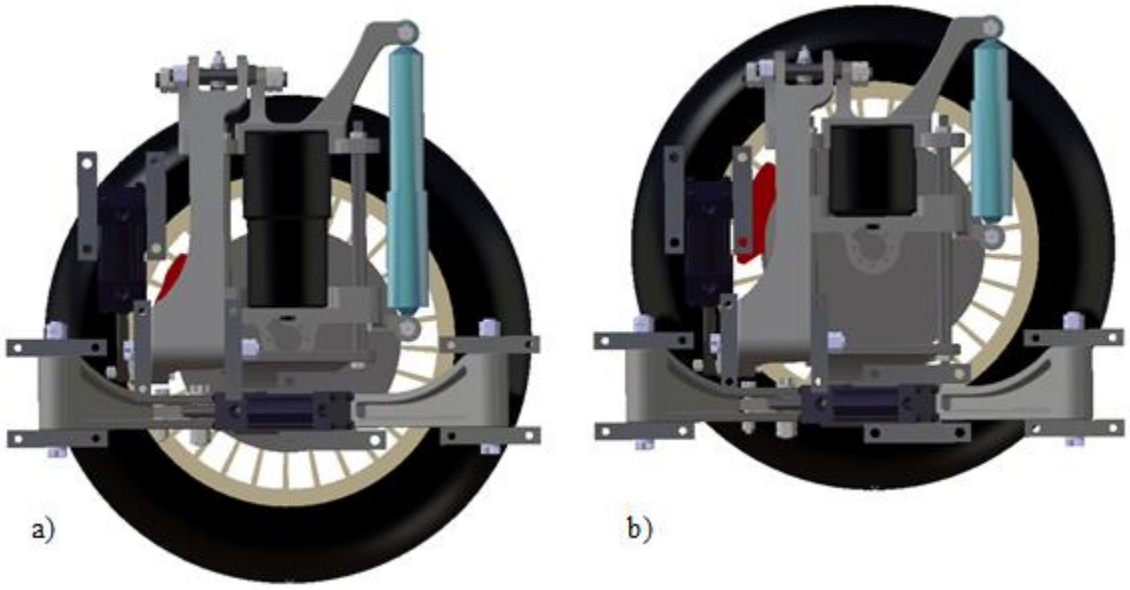

Figure 5-12: a) Suspension is extended 5 centimeter. b) Suspension is contracted 5 centimeter.

Figure 5-12 shows the wheel can move up and down vertically without affecting the steering or camber of the wheel. As a result, the suspension system is decoupled from the camber and steering mechanism. The floating spindle in Figure 5-13 is designed in a way that all the components of the wheel can be installed on it. The shaft of the in-wheel electric motor is connected to its front and is secured in place with seven bolts. There is a hole in the middle that allows the wires of the motor to go through and

connect to its drive. There are also dedicated spaces for the air spring and the damper. Moreover, the locations for four linear ball bushings are defined on the spindle, which allow for free movement of the spindle vertically along the rods. These bushings are held in place using retaining rings. There is also a bracket that holds the brake caliper. The brake disk is installed on the motor; as a result, this design makes sure there is no relative displacement between the brake disk and the brake caliper and ensures the entire wheel module moves together with the floating spindle.

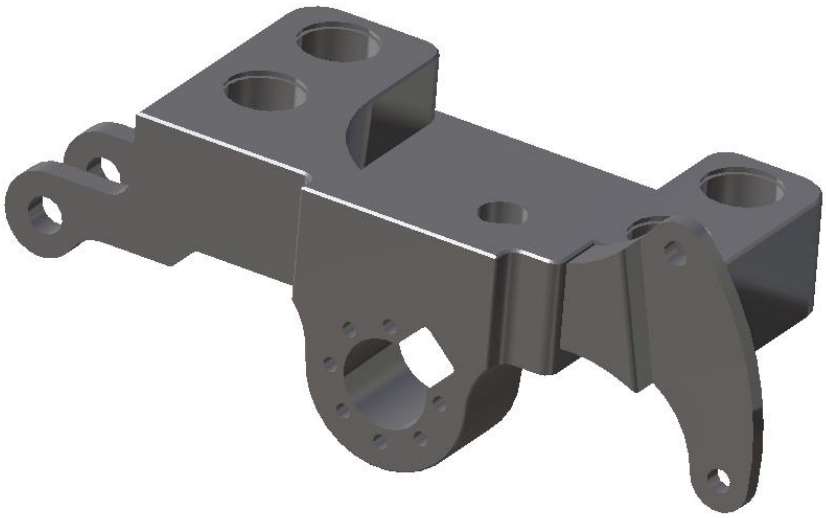

Figure 5-13: Floating spindle. In wheel motor and brake caliper are placed on the floating spindle so they move together.

The bottom spindle in Figure 5-14 is the connection between the suspension module and the steering mechanism. These two mechanisms have one degree of freedom relative to each other which is the rotation of the bottom spindle about the coupler of the four-bar mechanism. There is a bronze bushing press fitted in this part to ensure smooth rotation of the part. The intricate shape of the bottom spindle allows for all the movements of the steering and camber mechanism in a very compact space.

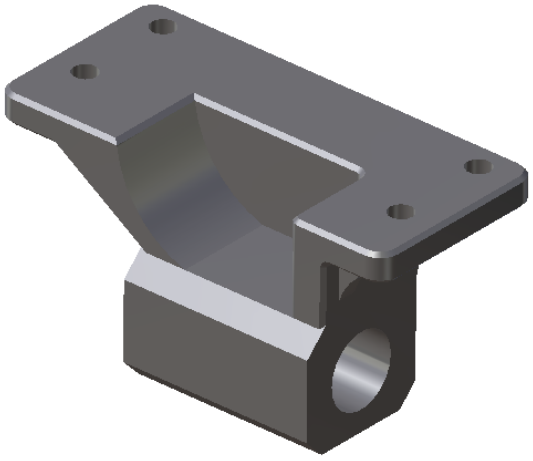

Figure 5-14: Bottom spindle. This part can rotate freely about the coupler of the four-bar mechanism.

Finally the top spindle in Figure 5-15 is designed to hold the damper and the spring in place. Additionally, it provides a connection bracket for the floating link. The shape is trimmed to ensure no internal collision occurs during maximum steering and camber.

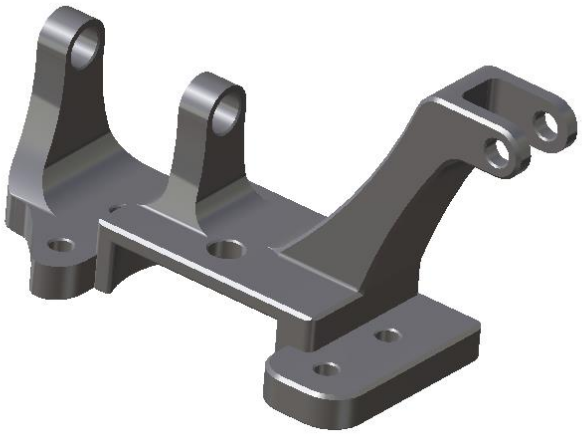

Figure 5-15: Top spindle. The combination of this part with bottom spindle and four vertical rods create a fixed frame relative to the wheel.

The top spindle, bottom spindle, and the four rods create a fixed frame relative to the wheel; whereas, the floating spindle which is rigidly connected to the wheel module can move freely with respect to this frame. Furthermore, the suspension mechanism ensures the chassis system isolates the vehicle from

road vibrations and provides a comfortable ride for the passengers. It must be noted that anti-vibration bushings are installed at all the connection points between the steering and camber mechanisms and the body of the vehicle. These rubber bushing isolate the body from the high frequency vibrations induced by the road.

In general in can be observed from Figure 5-16, the corner module can steer from -10 degrees to +10 degrees with maximum camber with no internal collision of the parts. These values are acceptable because at high speeds where maximum camber is needed the steering angles must be below 10 degrees in stable conditions.

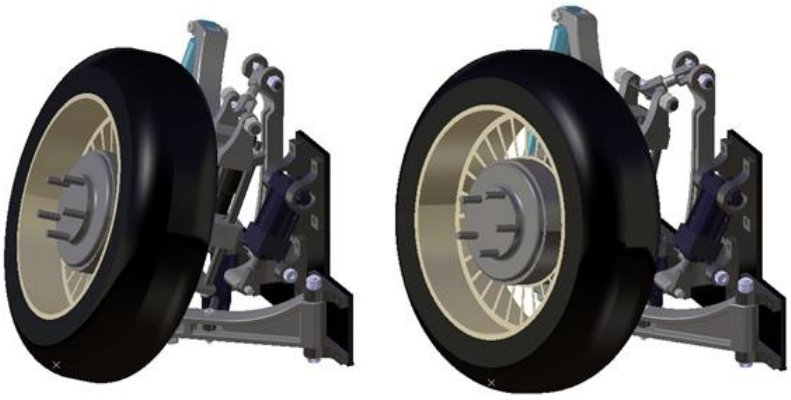

Figure 5-16; Isometric view of the corner module. This module can steer from 10 degrees to -10 degrees with maximum camber.

Figure 5-17: Side view of the corner module with maximum camber and maximum and minimum steering angles.

5.3 Finite Element Analysis

Finite element analysis was performed frequently during the design process and improvements were made as required. In this section only the finite element analysis on the final design is studied. As it was mentioned earlier, highest loading on the structure occurs when the lateral g force is exerted on the module at its maximum camber and maximum allowable steering in this configuration which is 10 degrees. Therefore, for finite element analysis the structure is studied in this configuration as well.

For the finite element analysis CATIAV5 was used. In order to do the analysis on the entire assembly, all the degrees of freedom are defined for the joints of the assembly. Instead of the modeling the air spring, the distance between the floating spindle and the top spindle was fixed. In static analysis the effect of fixing the distance using rigid links is the same as the effect of having an air spring in its compressed equilibrium position.

Moreover, to ensure the mechanism has no degree of freedom for movement, the length of the actuators were fixed. Because the specifications of the actuators indicate they can bear all the required forces, these actuators were excluded from the finite element model. Instead, two rods replaced these actuators to ensure the mechanism remains locked in its desired configuration. All the connection points to the vehicle body were fixed to satisfy boundary conditions of the model. Since actuators were not fully modeled, the ends of the rods were fixed instead of actuator body connections. Moreover, the load was applied at the location of the contact patch of the tire. This point is connected to the blots locations on the floating spindle through rigid links. This approach ensures all the forces, torques, and moments are transferred to the spindle properly.

In addition, the sizes of the bolts, pins and bushings are determined based on the load calculation from ADAMS; thus, available components in market that meet these load requirements are used. Consequently, these parts are excluded from the finite element model and are replaced by virtual components. Virtual components act as connections between two parts and provide necessary degrees of freedom for that joint. This approach significantly increases the processing time and ultimately generates the same results as the model with all the components included. A factor of safety of two is considered for the model to compensate for these simplifications.

For this application, 2^{nd} order tetrahedral solid elements were used. These elements have an advantage over brick elements for this application because they can capture all the non-linearity of the geometry and are suited for modeling curved shapes. The second order 10-node elements with fully integration formulation can calculate stress distribution within one element and are very accurate especially for

elastic deformations. However, they take more CPU time compared to 1st order tetra elements. The element size was selected to be 5 mm for this model.

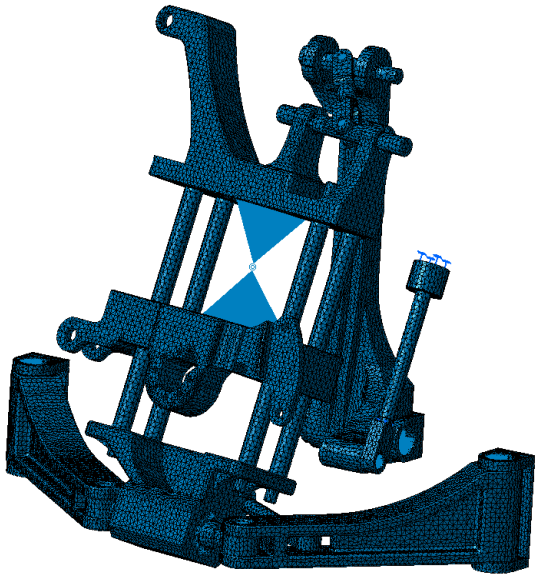

Figure 5-18: Full assembly of the corner module is meshed.

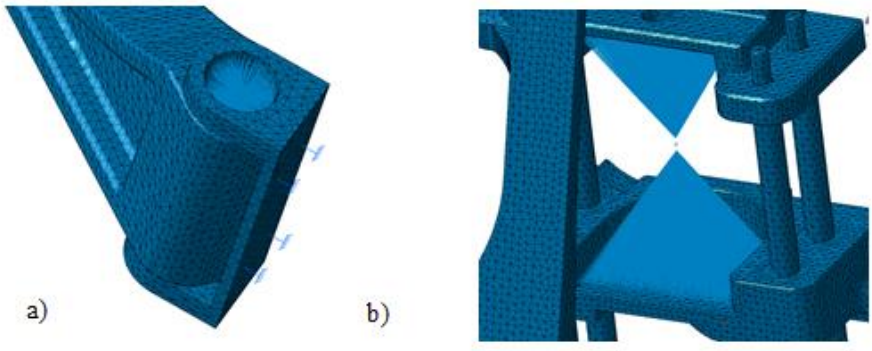

Figure 5-19: a) Virtual connection instead of the bolt which provides one degree of freedom for the steering arm about its axis relative to the chassis bracket. b) Virtual connection that simulates the air spring at its compressed position. The two surfaces cannot change their distance relative to each other.

Stress analysis results on the model are shown in Figure 5-20.This analysis was done statically in the linear elastic zone of the materials. This analysis calculates the von-mises stress within the material and failure should be considered with respect to material yield stress. This measure of stress is suitable for ductile materials such as metals.

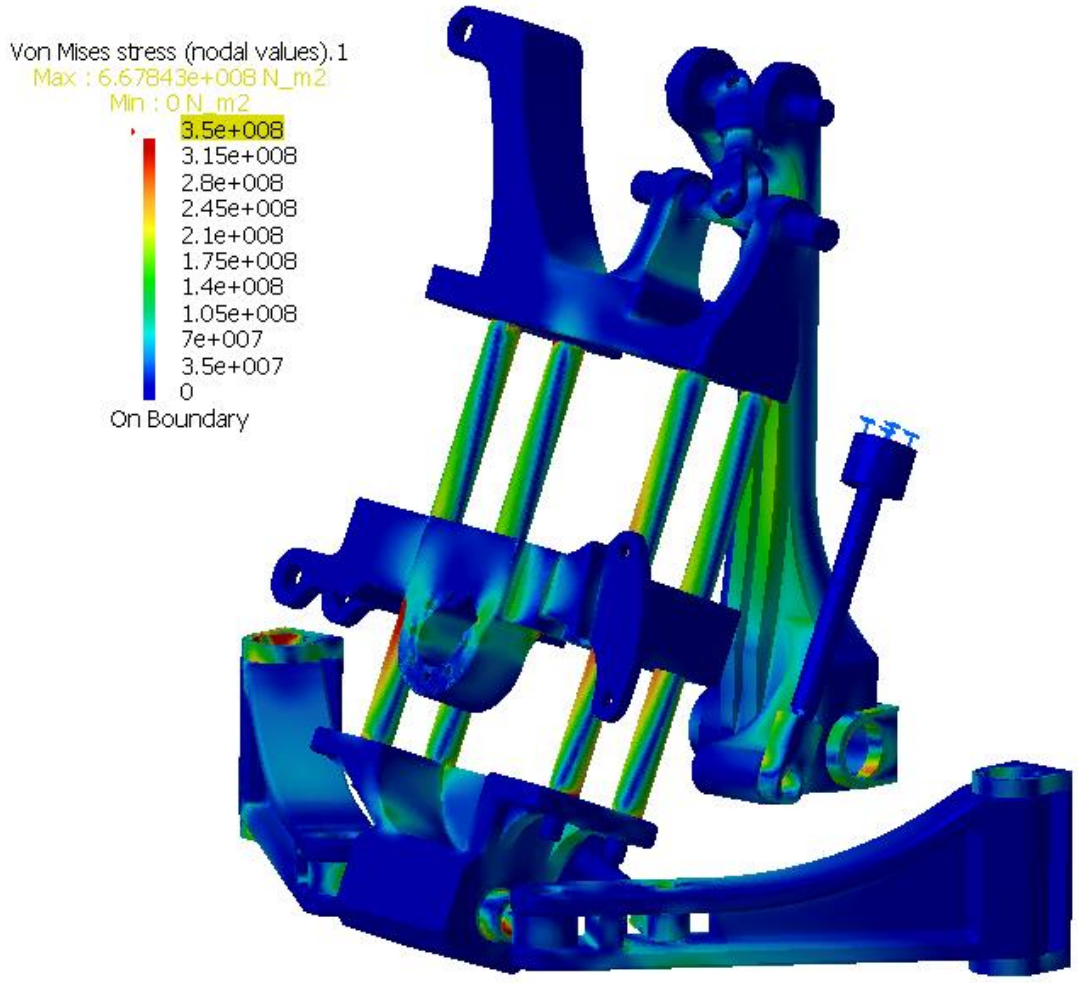

Figure 5-20: Stress analysis on the corner module mechanism.

It can be observed from Figure 5-21 that maximum stress happens on the coupler of the four-bar mechanism. However, it is interpreted that some of this stress is artificial and it is due to the fact that the lock nut was modeled as part of the coupler and the sharp edge acts as stress riser which contradicts

with reality. To be on the safe side the material for this part was selected as chrome plated high strength steel with yield strength of 700 Mpa. The validity of this selection was verified later by physical testing.

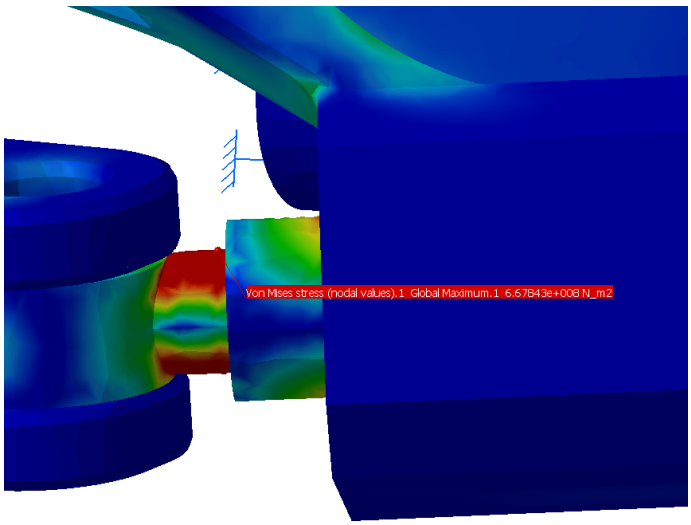

Figure 5-21: Maximum stress on the coupler pf the four-bar linkage.

Figure 5-22 shows that other areas with high stress are the vertical rods for the suspension mechanism. The maximum stress generated in these parts is 350 Mpa; as a result, the material of this part was also selected as chrome plated hard steel with yield strength of 700 Mpa. This value ensures the material remains in its elastic zone under worst loading conditions with a factor of safety of two.

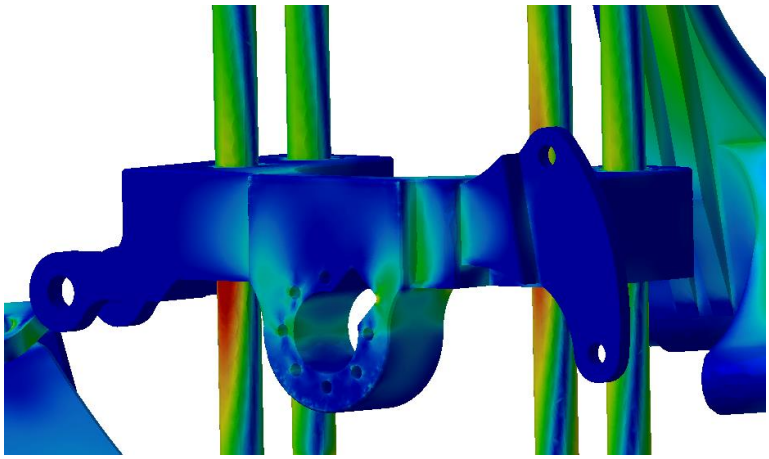

Figure 5-22: High stresses on the suspension sliders.

Finally it can be observed in Figure 5-23 that the third part with high stress is the camber link with a maximum stress of about 200 Mpa. Most of this stress is due to bending on this long member; as a result, two ribs were added to increase the moment of inertia of this part and decrease the amount of

stress in this part. The material for all other parts in the model was selected as aluminum 7075 with yield stress of 500 Mpa. This material ensures a factor of safety of more than two for this structure. Moreover, the density of aluminum is 2810 kg/m^3 as opposed to density of steel which is 7750 kg/m^3. Hence, this material ensures the structure is relatively light. Light weight is one of the main criteria for electric vehicle designs to achieve energy efficient vehicle.

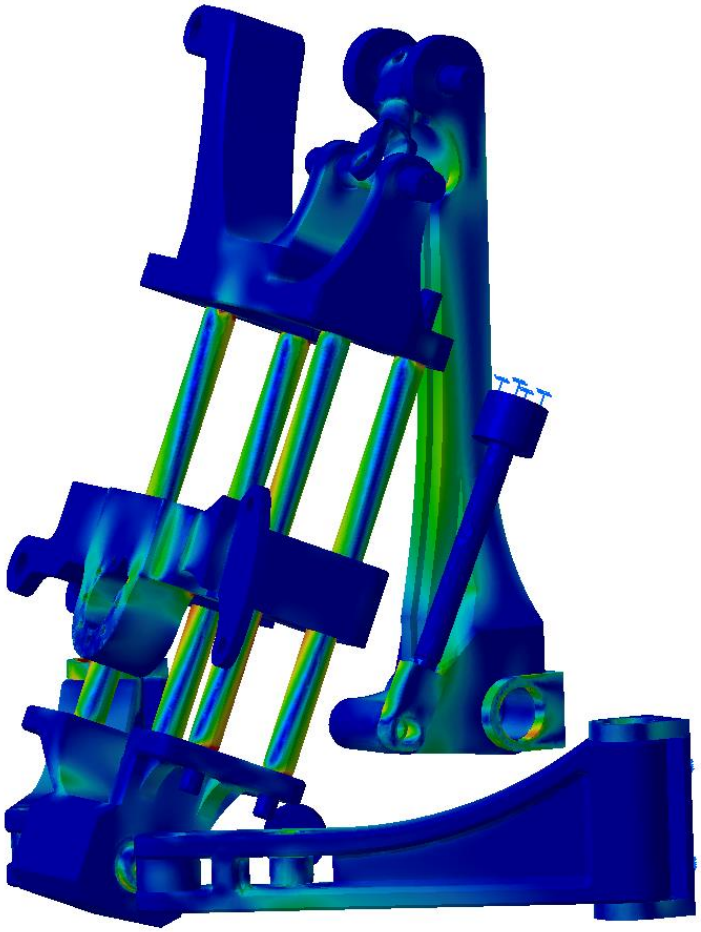

Figure 5-23: High bending stress on the camber link.

At this stage, the design of the corner module is finalized. This design meets all the packaging, steering, camber, and suspension requirements. Moreover, stress analysis shows the module bears highest possible loads induced by the road or minor impacts.

Chapter 6
Fabrication and Experimental Studies

The goal of this project is to fabricate a corner module that can be installed on the vehicle. The first step was to build a scaled down prototype to ensure that the physical prototype works the same as the simulations. After validation, the full size prototype is built and its kinematic is verified for this project.

6.1 Scaled down prototype

In order to build the scaled down version prototype, a 3D-printed model was used. In this model all the degrees of freedom were allowed to ensure the kinematic works as expected. Moreover, the other objective of building this prototype was to ensure there is no physical limitation for assembling the components, which might not be realized from solid models and simulations.

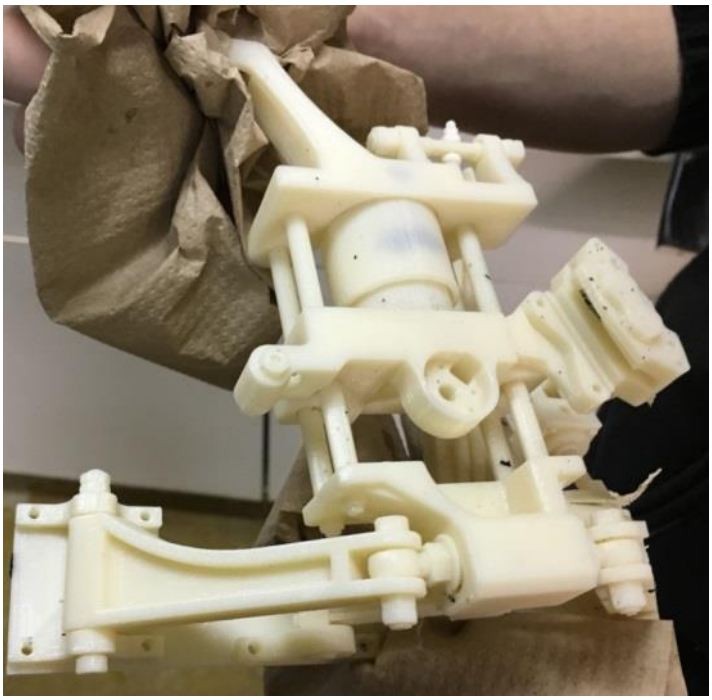

Figure 6-1: 3D-printed scaled down version of the corner module.

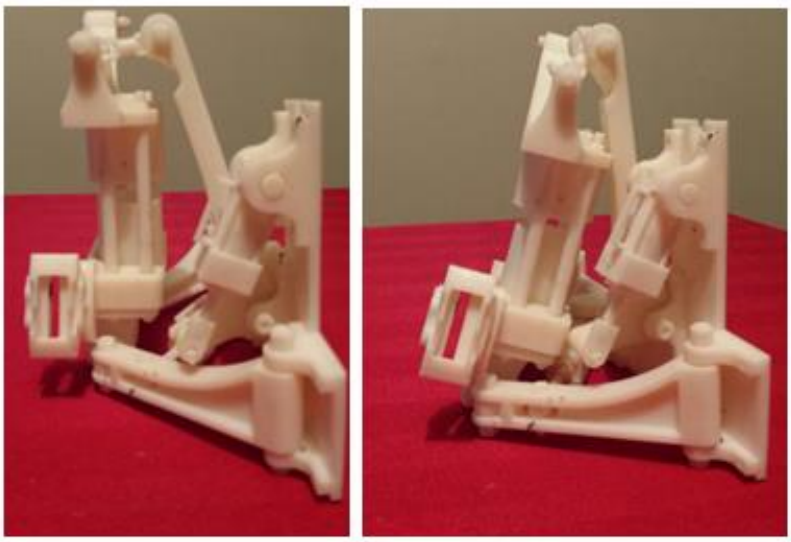

Figure 6-2: The camber mechanism works same as the simulations.

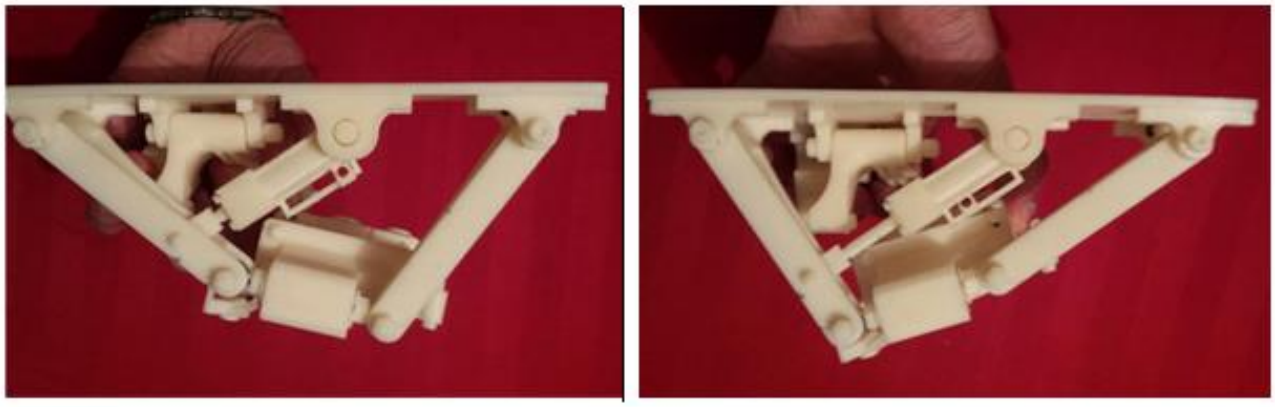

Figure 6-3: Steering mechanism works the same as the simulations.

Figure 6-2 and Figure 6-3 show the 3D-pritend prototype of the corner module's mechanisms. It was validated that these mechanism worked as expected and all the displacements and angles were measured by hand to ensure the mechanisms behave similar to the simulations. Furthermore, by inspection it was evident that there is no restriction on assembling the components of the corner module.

It should be noted after building this prototype, the design for the floating spindle was altered moderately to ease the manufacturing of this part.

6.2 Full size prototype

Once the design was verified by the 3D-printed prototype, the next step was to build the full size prototype. In order to fabricate the first prototype, all the links were built out of aluminum 7075 blocks using CNC machines and the rest of the off-shelf components were ordered for this application.

Figure 6-4: Components of the corner module before assembly.

These parts are shown in Figure 6-4 and were put together and the final assembly of the corner module was made as illustrated in Figure 6-5.

Figure 6-5: Assembly of the corner module mechanisms.

All the parts of the module can be assembled easily. In addition, when all the components are assembled, each part is accessible which greatly helps with maintenance of the module. For instance, this design ensures that brake pads are accessible without disassembling the wheel, or the air spring can be inflated with ease.

Figure 6-6: Steering mechanism and camber mechanism of the corner module.

As it can be observed in Figure 6-6, the locations of the actuators provide enough space to install required sensors and routing of the hoses are feasible as well. Finally, the bushings for the actuators' mounts were modified later to fit in the assembly as required.

Figure 6-7: In-wheel motor is connected to the rim by spokes.

For this application, instead of using a styled rim, the electric motor was attached to the tire using spokes. This approach saved space to meet the compact design requirements; more importantly this configuration is much lighter than available rims in the market. As a result, the un-sprung mass to sprung mass ratio is less for this design; hence, a higher ride quality can be achieved.

6.3 Kinematic validation of the design

In order to validate the kinematics of the design, a test setup was needed to be built. This set up has to replicate the chassis of the vehicle. For this purpose, a stand was designed and installed on the available bed plate in the lab (University of Waterloo Mechatronic Vehicle Systems Lab). This stand is illustrated in Figure 6-8 and it was required to be very sturdy in order to withstand high loads applied on the corner module. Moreover, because the entire stand would be very heavy as one piece, some of the pieces are bolted together; ergo, they can be detached and moved with less effort.

Figure 6-8: Gantry test structure for the corner module. This piece represents the chassis of the vehicle where the corner module is installed on.

It can be observed from Figure 6-8 that the stand fits properly on the available bed plate in the lab. This compact test setup allows other tests to run alongside the corner module on the same bed plate.

On an actual vehicle, all the loads from the road are applied to the contact patch of the tire. In general, for testing purposes with a fixed stand a moving platform is required to simulate road behavior. However, these moving platforms are very costly and not widely available. Because no moving platform was available in the lab, another approach was taken to apply required loads to the corner module. For testing, another part was designed to replace the wheel and tire. As a result, the entire required load from the road including vertical, longitudinal, and lateral loads could be applied to this part at the location of the tire contact patch. The design of this part is depicted in Figure 6-9.

Figure 6-9: Replication of the wheel so all the forces in different directions can be applied at the location of the contact patch of the tire.

This wheel replica sits on the floating spindle where the in-wheel motor is supposed to be installed. Three actuators exert force in three different directions to simulate road forces on the tire as illustrated in Figure 6-10.

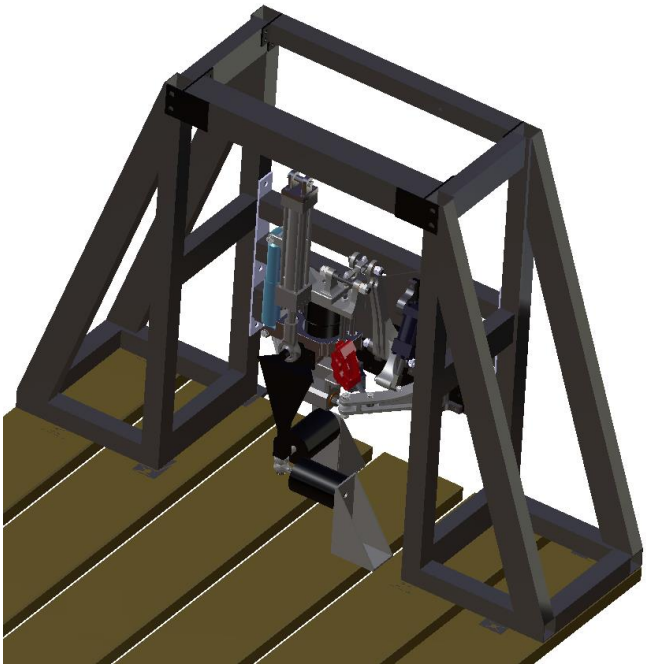

Figure 6-10: isometric view of the test setup for the corner module.

One actuator applies vertical load to this part. The line of action of this actuator passes through the location of the tire's contact patch. This configuration ensures vertical forces and torques applied to the corner module mechanisms are similar to the ones applied to the contact patch from the road.

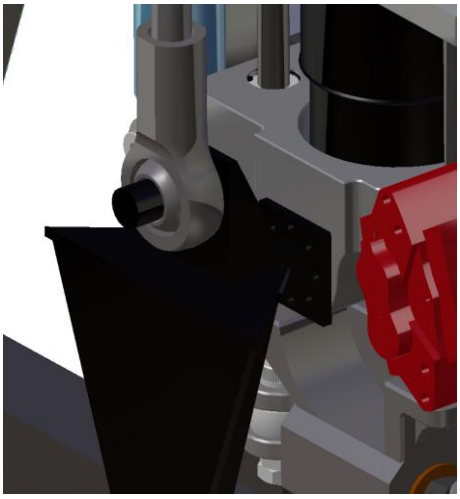

Figure 6-11: Vertical cylinder is connected to the wheel replica to exert vertical forces.

At the bottom of this part, there are two other actuators that apply longitudinal and lateral forces at the location of the tire's contact patch. Instead of hydraulic actuators two air springs were selected for this application. Air springs can deform and adjust their orientation based on the location of the contact patch during different steering and camber angles.

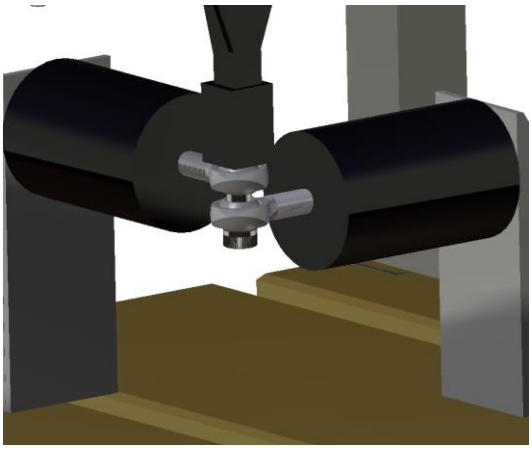

Figure 6-12: Two air springs are connected to the replication of the wheel to exert longitudinal and lateral forces at the location of the contact patch of the tire.

Figure 6-13 shows the fabricated part that replicates the wheel for testing purposes.

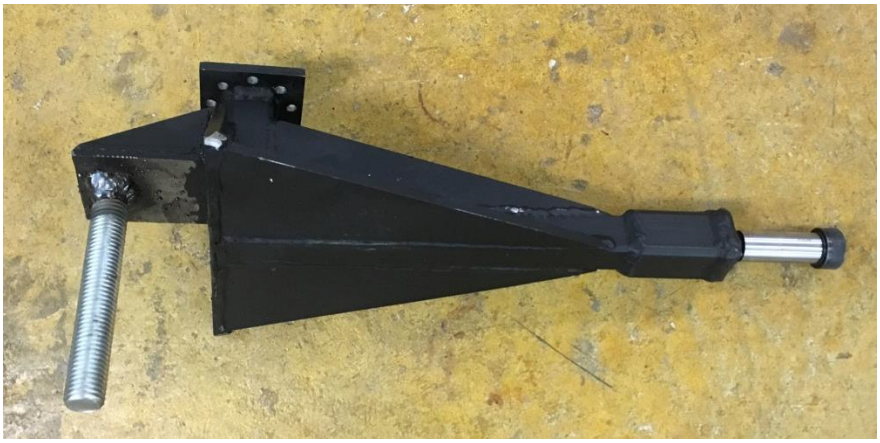

Figure 6-13: fabricated part that sits instead of the wheel.

The test setup for the corner module is illustrated in Figure 6-15. The back plate of the module sits on the test stand and one vertical actuator and two air springs exert required forces to the mechanisms in three different directions.

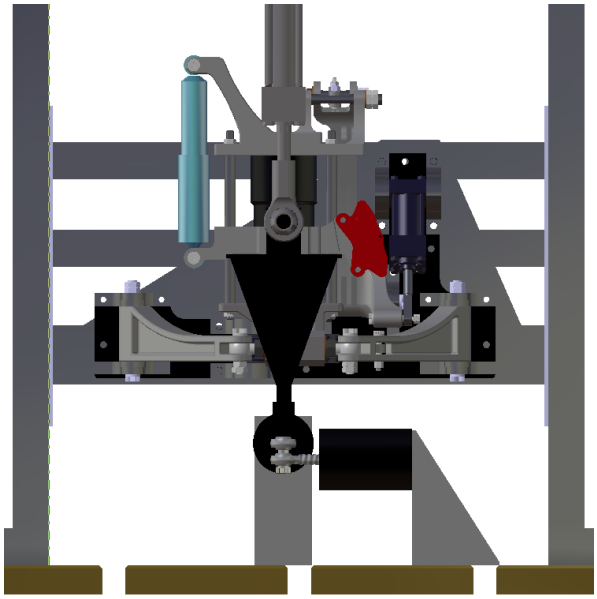

Figure 6-14: Front view of the corner module on the test setup with actuators to exert loads on the assembly.

This set up was built in the lab to allow validation of the kinematics for both steering and camber mechanisms of the corner module.

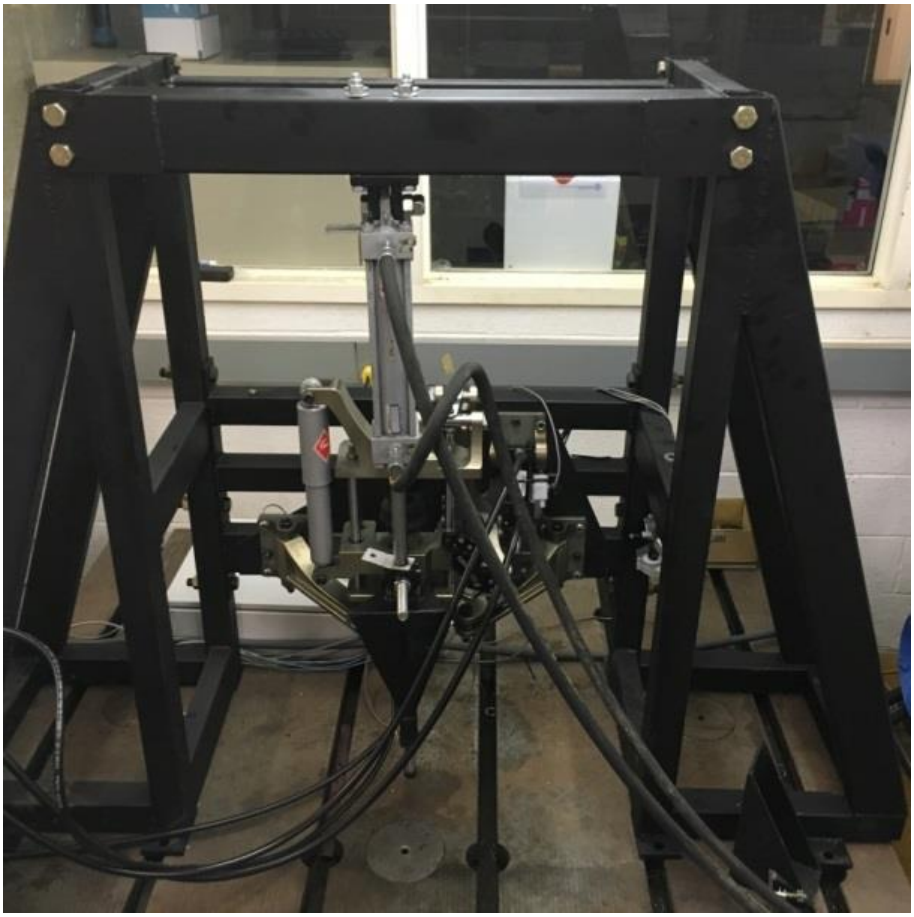

Figure 6-15: Test setup of the corner module in the lab.

In order to drive the actuators, a hydraulic circuit was built. The drivers for the actuators are two steering valves which are driven by stepper motors. Stepper motors are controlled through micro stepper controller that detects the rising edges of input signal to drive the motor. As a result, a PWM approach was taken to control the speed of the motor; hence, the flow rate of the valves corresponds to speed of the actuators.

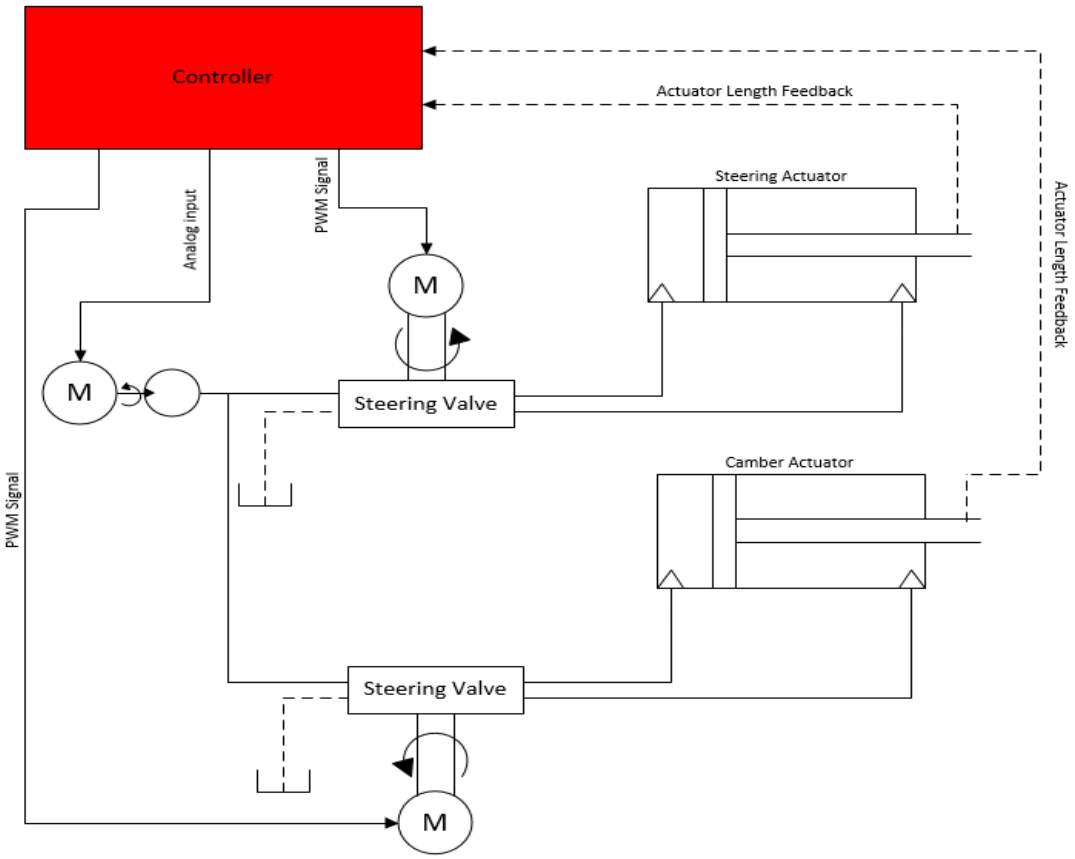

Figure 6-16: Hydraulic circuit and controller designed to drive the actuators.

Figure 6-17: Stepper motor driving the steering valve.

The entire system is being controlled through a PLC. For this application, a Beckhoff controller and modules were selected as the PLC control unit. The control panel reads the sensors signal and provides digital signals in square wave form to the stepper motor drives.

Figure 6-18: Beckhoff control panel.

To get feedback on the length of the actuators analog string pots were installed on them as depicted in Figure 6-19.

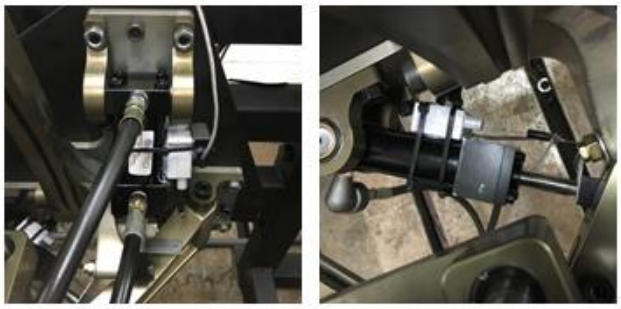

Figure 6-19: Linear potentiometers installed on the actuators to provide feedback on the length of the actuators.

Validation tests were run to ensure the kinematics of the module work as expected. In Figure 6-21it can be observed the module is capable of providing required steering angles and camber angles.

Figure 6-20: Corner module on the test stand in its nominal position at zero steering and zero camber.

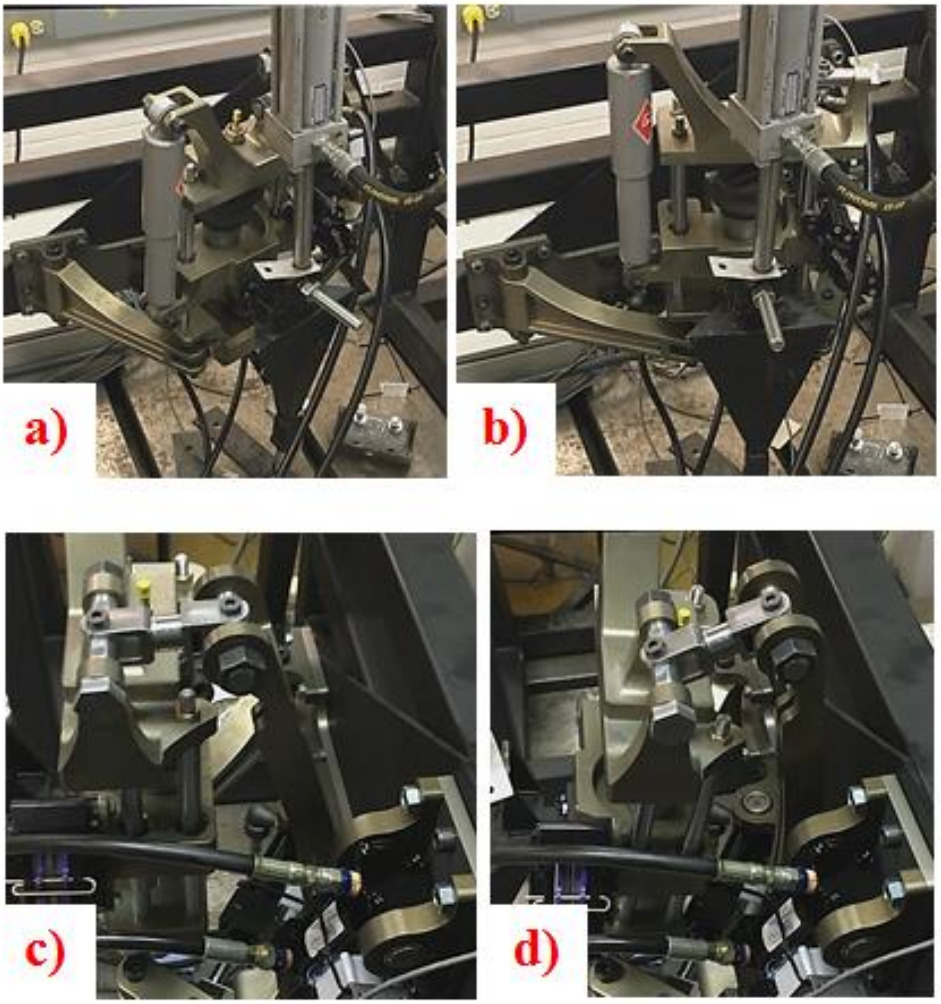

Figure 6-21: a) Corner module at 20 degrees steering. b) Corner module at -20 degrees steering. c) Corner module at zero camber. D) Corner module at -15 degrees camber.

In order to experimentally validate the kinematics of the corner module, an "Optotrak vicra" was installed on the test setup. This device can measure the orientation of the wheel independent of the actuator lengths. Therefore, both the steer angle and camber angle can be measured to verify the design. In the setup, the camera detects the orientation and location of the marker in its initial position. Thereafter, any change in the orientation of the marker is measured by the cameras. As a result, the amount of steer angle and the camber angle can be measured at any configuration for the mechanism.

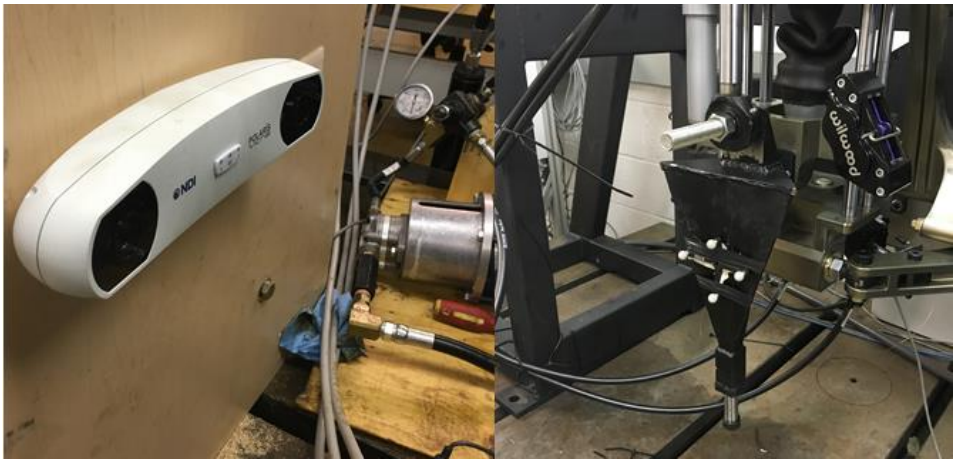

Figure 6-22: Optotrak Vicra. In the left the camera is installed. On the right the marker is attached to the wheel to measure its orientation in space.

The control system receives a desired position for the steer angle and camber angle. Then using a lookup table it drives the actuators to their calculated lengths that satisfy the required angles. The lookup table was made based on the simulations' results. In order to validate that using the lookup table the desired position is obtained correctly, the steer angle and camber angle were measured using the optotrak. The collected results from the optotrak were correlated with simulation results.

The results of the tests are shown in Figure 6-23 and Figure 6-24. Based on the actuator lengths the simulated angles and the actual angles are graphed. It should be noted that the outliers of the tests' data are excluded from the results.

From Figure 6-23 it can be observed that the test results are very close to the simulations. There is insignificant difference between the two. This discrepancy is due to the compliance of the steering mechanism. The simulations are based on rigid body assumption, whereas there are deformable components in the actual mechanism such as rubber bushings between the mechanism and the chassis system.

Figure 6-24 also shows acceptable results for the camber mechanism. The accuracy of the camera cannot capture small variations in camber angle. As a result, it can be seen the captured data is noisy. However, the linear fitted curve between the test points follows the simulations very closely and shows the same trend as the simulations.

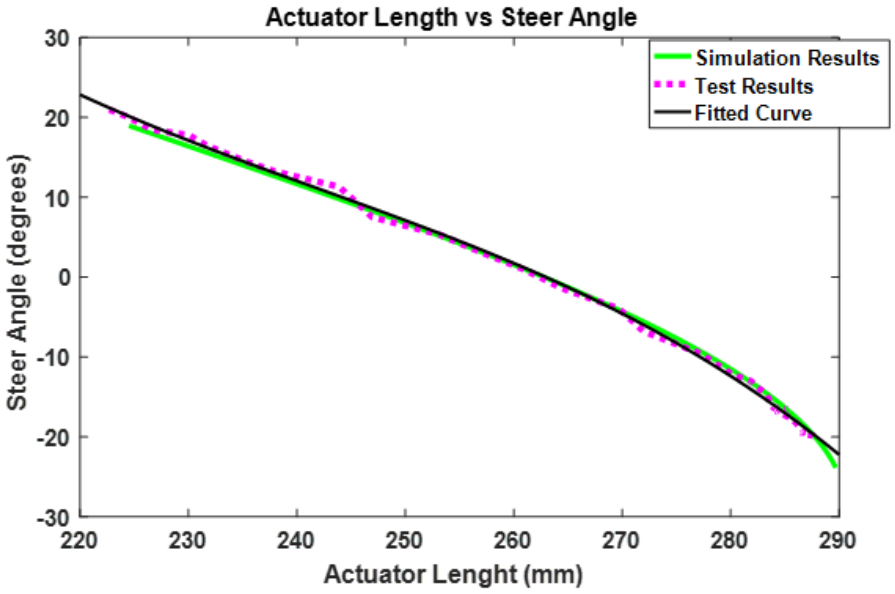

Figure 6-23: Steer angle test results and simulations

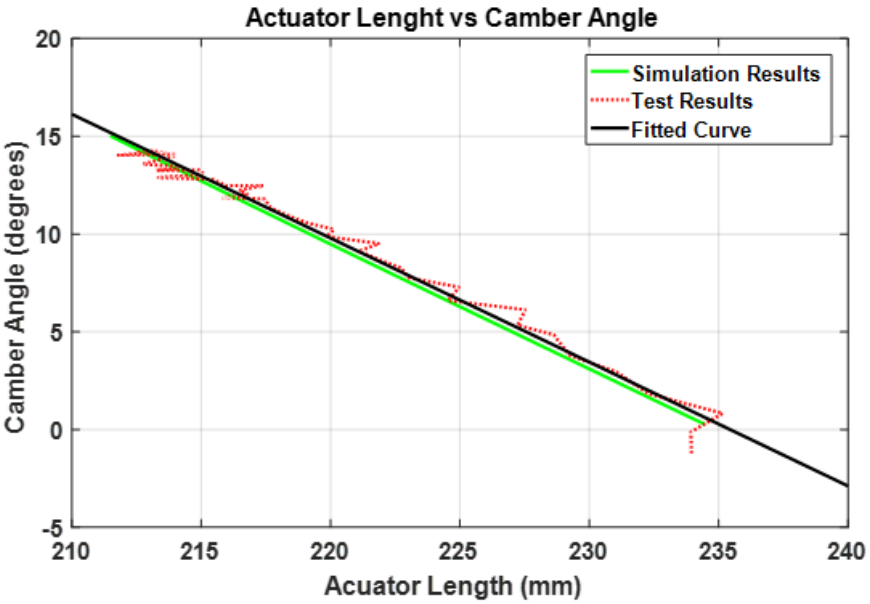

Figure 6-24: Camber angle test results and simulations

The system noise is more obvious when the range of camber variation is very small. This effect can be seen in Figure 6-25 where the camber angle is measured as the steering angle changes. Three cases for "camber by steer" were studied at different initial camber angles, then the steering angle was changed in its acceptable range to capture camber variations of the wheel. At high camber angles the range of

steering is between -10 to 10 degrees as it was discussed in the previous chapter. Whereas, the steering range at zero camber angle is -20 to 20 degrees. Since the camber variation is minor, it can be seen that the camera could not capture the correct camber angles. Therefore, the test results demonstrate a flat line as opposed to the decreasing trend of the simulated lines. As a result, the test results are not reliable for validation in the case of camber by steer. However, it can be seen that camber by steer is insignificant for the corner module in both simulations and tests which is desirable for the chassis system.

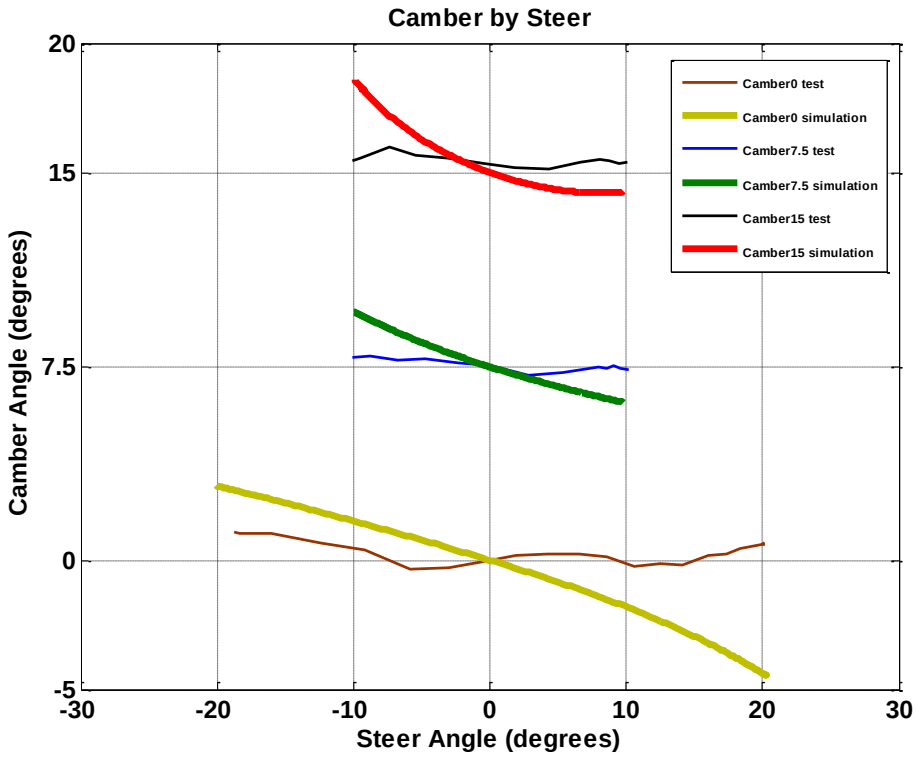

Figure 6-25: Camber by steer at different initial camber angles

This validation results show the corner module works as expected in terms of steering mechanism and camber mechanism. Moreover, it was shown during the tests that the actuators can generate enough force to operate the system fast enough. As a result, the corner module is ready to be tested on a test vehicle.

Chapter 7
Design Improvement Using Optimization

Up until now this thesis has introduced a new design for corner modules. This chapter proposes an optimization method that can be utilized to find the location of hard points for the next generation of this corner module design to improve its performance.

In order to find the hard points of the corner module in an optimized manner Genetic Algorithms (GA) is utilized. GA is considered as a suitable method for global optimization. By having a large population, GA ensures the global minima is found and it does not get stuck in any local minima [37]. The outputs of the GA optimization are the spatial locations of the hard points for a given objective function. It was discovered that packaging requirements of the corner module impose serious constraints on the locations of these hard points. As a result, the current locations of the hard points that satisfy the packaging requirements are used as the initial conditions for the GA function. Furthermore, spatial constraints are defined around these points, which allow the GA to find the best possible answer for each point within the space defined around them.

As it was discussed in Chapters 3 and 4, the important factors for any chassis system are the effects of the kingpin axis, the amount of wheel travel, and the camber by steer behavior of the wheel. Therefore, multiple objectives functions for the GA are defined as presented in equations (8-1) to (8-5).

The first objective function is the amount of scrub radius. This is the lateral distance between the contact patch of the tire and the intersection of the kingpin axis with the ground. The squared of this value is measured to ensure the value is always positive. Moreover, this objective function considers the summation of instantaneous scrub radius values throughout the steering range. In equation (8-1), $Y_t$is the lateral coordinated of the tire and Y_{ICG} is the lateral coordinate of the instantaneous center of the wheel on the ground, n is also the number of points that define these variables are measured during steering. Each step adds one degree to the steering angle.

$$obj1 = \sum_{1}^{n} (Y_t(i) - Y_{ICG}(i))^2 \tag{8-1}$$

The second objective function is the mechanical trail. This is the longitudinal distance between the contact patch of the tire and the intersection of the kingpin axis with the ground. As it was explained in Chapter 3, positive value for this measure is desired. As a result, the second objective function is defined so that this value is positive at high speeds where the steering angle is between -5 to 5 degrees. In this function, $X_t and\ X_{ICG}$ are the longitudinal coordinates of the tire and the instantaneous center of rotation

of the wheel on the ground respectively. The difference is measured against 4 cm which was found to provide good results by trial and error.

$$obj2 = \sum_{1}^{n} (X_{ICG}(i) - X_t(i) - 0.04)^2 \tag{8-2}$$

Other objective functions are defined to minimize the wheel travel on the ground in both lateral and longitudinal directions as well as camber by steer as defined in equations (8-3),(8-4), and (8-5).

Longitudinal wheel travel: $$obj3 = X_{tmax} - X_{tmin} \tag{8-3}$$

Lateral wheel travel: $$obj4 = Y_{tmax} - Y_{tmin} \tag{8-4}$$

Camber by steer: $$obj5 = \sum_{1}^{n} (Camber(i))^2 \tag{8-5}$$

As a result, the objective function that is minimized by the GA must contain all the above objective functions as follows:

$$obj = w_1 obj1 + w_2 obj2 + w_3 obj3 + w_4 obj4 + w_5 obj5 \tag{8-6}$$

where w_i's are the weights associated with each function. In this thesis, the weights are given as $w_1 = 20, w_2 = 10$ and $w_3 = w_4 = w_5 = 1$. It was found by trial and error that these weights provide desirable results for the corner module.

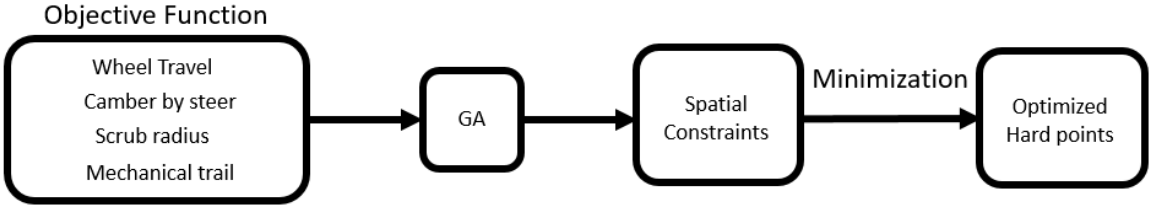

Figure 7-1: Optimization process flow

Based on the optimization process in Figure 7-1 the hard points of the chassis system are found as tabulated in Table 7-1.

Table 7-1: Coordinates of optimized hard points

Optimum Points	O	A	B	C	Q	P
x-coordinate (mm)	0	0.1668	0.3414	0.5082	0.2051	0.1885
y-coordinate(mm)	0	0.2115	0.2115	0	0.0873	0.2007
z-coordinate(mm)	0.1799	0.1799	0.1799	0.1799	0.5425	0.5583
Non Optimum points						
x-coordinate (mm)	0	0.185	0.375	0.560	0.210	0.210
y-coordinate(mm)	0	0.200	0.200	0.0	0.93	0.200
z-coordinate(mm)	0.165	0.165	0.165	0.165	0.600	0.600

Using these points, the locus of the tire's contact patch and the intersection of the kingpin axis with ground is calculated for full steering range from -20 to 20 degrees. This locus is illustrated in Figure 7-2. It can be observed the behavior of the steering system has a similar pattern to the current design and this is due to the fact that the optimization has been done around the current locations of the hard points. A more in depth analysis is done in section 7.1.

7.1 Comparison of the current design with the optimized design

In this section a comparison is done between the current design and the optimized design resulted from the GA. The contact patch behavior is shown in Figure 7-2 for both the current design and the optimized design.

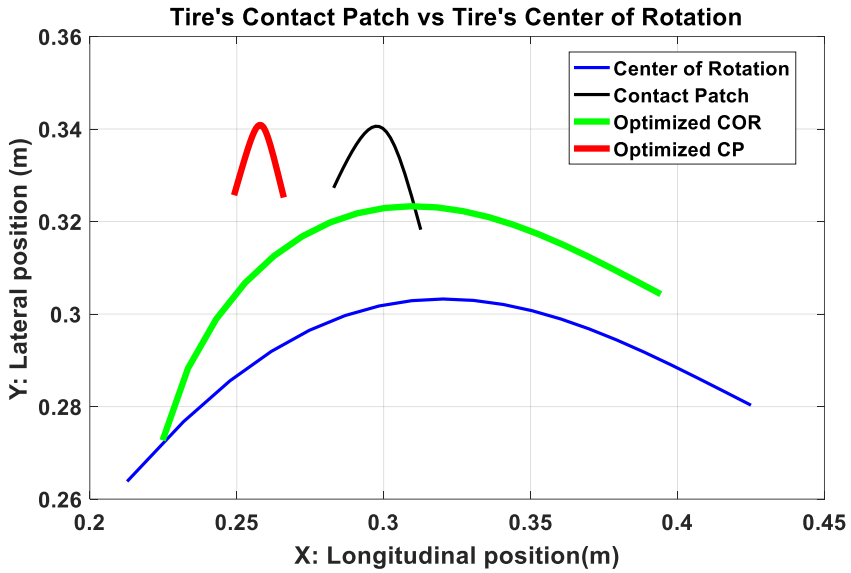

Figure 7-2: Locus of tires contact patch and its center of rotation on the ground

It can be observed the tires' travel during full steering range is less for the optimized design. Moreover, the center of rotation of the tire on the ground moves closer to the contact patch. In Figure 7-3 it can be observed that the amount of scrub radius for the optimized design is considerably smaller. This phenomenon minimizes the toe effect on the wheels which reduces the magnitude of the forces on the steering actuator.

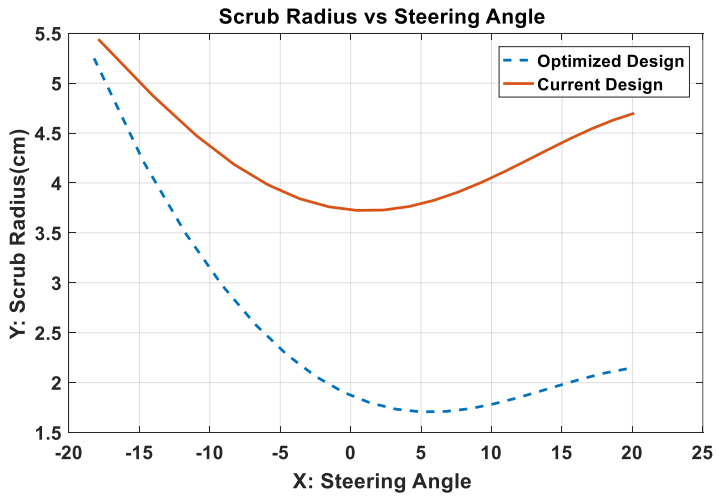

Figure 7-3: Scrub radius is full steering range

Figure 7-4 shows that the mechanical trail is positive in the optimized design from -7.5 to 20 degrees of steering angle. This configuration provides directional stability for the wheel at high speeds as

discussed in Chapter 3. The corner module is capable to actively provide directional stability and minimize the toe effect. However, the optimized configuration provides passive stability for the corner module and makes it fail safe as well. It can be seen that at zero steering the amount of mechanical trail is 4 cm as defined in the objective function. Since for the dual four-bar configuration of the corner module the instantaneous center of the wheel on the ground moves in the opposite direction than the tire contact patch, the mechanical trail is negative at some steering angles. This value can be always positive by changing the 4 cm parameter to a higher value. However, this results in a very high mechanical trail at 20 degrees of steering angle. A very high value is not desirable because it requires a lot of force for the actuator to rotate the wheel. Therefore, 4 cm was chosen which provides a reasonable positive mechanical trail at high speeds where directional stability is more important.

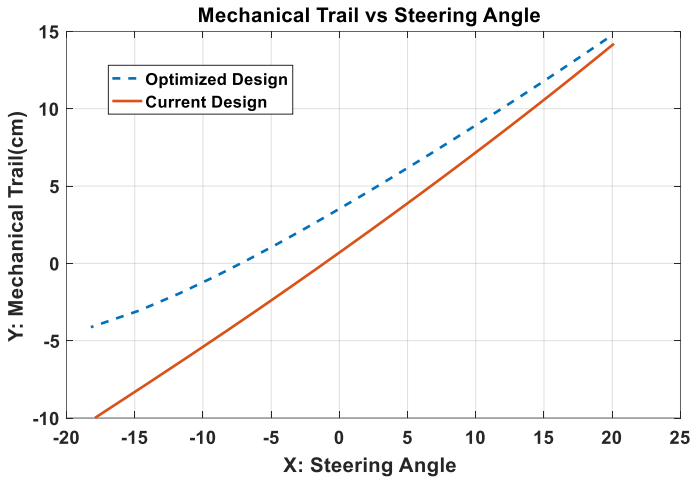

Figure 7-4: Mechanical trail in full steering range

Figure 7-5 demonstrates the behavior of the steering angle as the angle of the steering arm of the four-bar linkage changes. This behavior is similar to the current design; however, the curve shows a more linear behavior which is desirable for controlling the corner module. Moreover, it can be seen that the

steering spindle is farther from its singular points, which considerably reduces the amount of forces on the steering actuator.

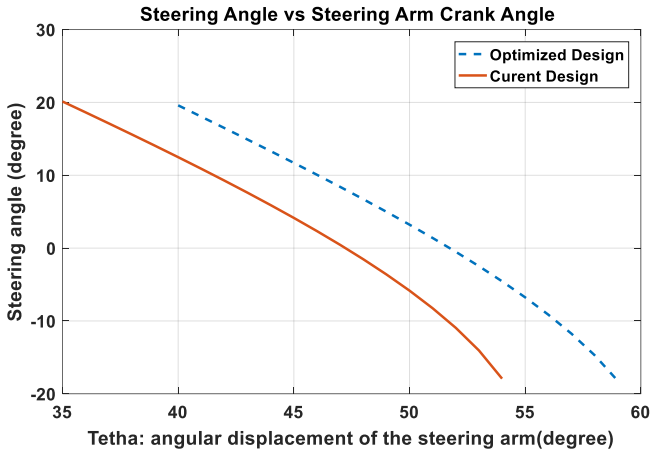

Figure 7-5: Steer angle range

Camber by steer for the optimized design performs slightly worse than the current design as depicted inFigure 7-6. This graph shows that the magnitude of camber change is more sensitive to steering angle. For this design the amount of camber by steer is acceptable. In this section more priority was given to scrub radius and mechanical trail. However, higher priority can be given to camber by steer for a different design at the cost of having a worse scrub radius and mechanical trail.

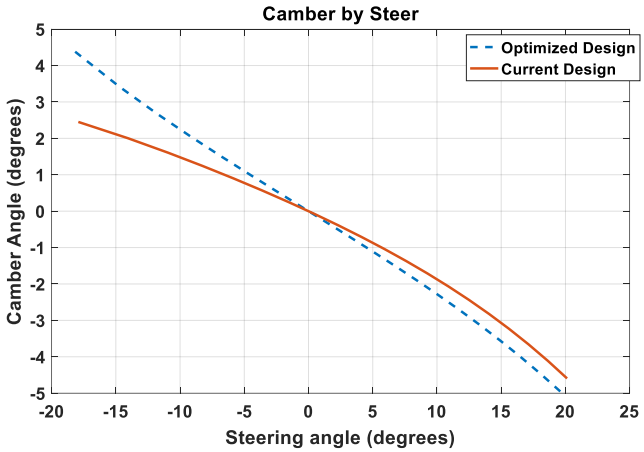

Figure 7-6: Camber by steer

Chapter 8
Conclusion and Recommendations

This thesis proposed a new wheel corner module for narrow urban vehicles. All the packaging constraints, camber, and steering requirements were established based on the chassis design of a three-wheeled vehicle. This compact design coupled with x-by-wire technology can be applied to other vehicles and significantly simplify the complex design and assembly process of vehicles' chassis. Implementing this module results in eliminating steering links and drive shafts, hence creates more room that can be used for passengers comfort and safety. This new design improves the shortcomings of the existing designs in the market as discussed. The contributions of this thesis are highlighted below:

- This thesis introduced a new steering mechanism using a four-bar linkage for the first time. Utilizing this mechanism allows for better load distribution and realization of corner modules.
- A novel active camber mechanism integrated with suspension mechanism was implemented in this corner module that can improve the rollover threshold of narrow vehicles and increase their safety.
- The combination of this steering mechanism with the camber mechanism results in creation of a virtual kingpin axis and a method to define this axis was defined. This kingpin axis can be used to passively meet the stability requirements for the chassis systems.
- This approach allows for a highly compact design of the corner module. Moreover, fabrication of the full sized prototype demonstrated that assembly and maintenance of this module is simple.

It is worth noting that more studies are needed for implementation of the proposed module on vehicles. The recommendations for future works are:

- A nonlinear model for the vehicle can be built to study the effect of camber on its rollover behavior with more accuracy.
- The effect of this module on vehicle dynamics can be investigated through torque vectoring and active steering.
- A thorough study can be done on the steer-by-wire and brake-by-wire systems and their feedback methods to the driver.

Bibliography

[1] Department of Economic and social Affairs, "World Urbanization Prospects," The united Nations, 2014.

[2] "Global Transport Scenarios 2050," World Energy Council, London-United Kingdom, 2011.

[3] "Electric Vehicles in 2013: A Progress Report," Transpot and Environment (T&E); Project lead: Greg Archer, July 2014.

[4] N. M. H. N. D. G. a. S. L. A. Santos, "Summary of Travel Trends: 2009 National Household Travel Survey," U.S Department of Transportation; Federal Highway Administration, pp 33, June 2011.

[5] "Michelin Active Wheel, Press Kit. 10/2008. Paris Motor Show. Michelin.[Accessed 9.6.2010].".

[6] P. Evans, "gizmag," 2 December 2008. [Online]. Available: http://www.gizmag.com/michelin-active-wheel-production-electric-car-by-2010/10489/. [Accessed 19 June 2016].

[7] N. D'Este, "Gommeblog.it," 10 June 2010. [Online]. Available: http://www.gommeblog.it/news-gomme-e-cerchi/5457/michelin-active-wheel/. [Accessed 19 June 2016].

[8] M. S. D. W. Daniel Laurent, "Unit comprising a wheel and a suspension integrated in the wheel hub". Europ Patent Publication Numer: EP0878332 B1, Application Number:EP19980107687, 10 Jul 2002.

[9] M. S. Daniel Laurent, "Vehicle suspension having active camber variation". US Patent Publication number: US6170838 B1, Application number: US 09/078,052, 9 Jan 2001.

[10] technical innovations, "Siemens VDO drives toward the future," *SAE OHE,* p. 6, October 2006.

[11] H. S. K. N. Y. o. C. C. H. J. S. M. L. H. L. S. In Su Kim, "Electronic Wedge Brake System". US Patent Publication number: US20100140028 A1, Application number: US 12/507,579, 10 Jun 2010.

[12] Hiriko driving mobility, "www.hiriko.com," [Online]. Available: http://www.un.org/esa/dsd/susdevtopics/sdt_pdfs/meetings2012/statements/espiau.pdf. [Accessed 19 June 2016].

[13] W. J. M. Peter Alfons Schmitt, "Autonomous modular vehicle wheel assembly". US Patent Publication number: US8757309 B2, Application number: US 12/492,128, 24 Jun 2014.

[14] B. Bluethmass, "ntrs.nasa.gov," 7 April 2015. [Online]. Available: http://ntrs.nasa.gov/archive/nasa/casi.ntrs.nasa.gov/20150004599.pdf. [Accessed 19 June 2016].

[15] J. a. B.Bluethmann, "ntrs.nasa.gov," 17 Nov 2015. [Online]. Available: http://ntrs.nasa.gov/search.jsp?R=20150019646. [Accessed 19 June 2016].

[16] S. ZETTERSTRÖM, "Wheel suspension arrangement in a vehicle". Europe Patent EP1144212 B1, 7 Jul 2004.

[17] S. Zetterström, "Electromechanical Steering, Suspension, Drive and," *IEEE*, vol. 2, no. 0-7803-7467-3, pp. 1856-1863, 2002.

[18] S. A. A.Khajepour, Electric and Hybrid Vehicles, Technologies, Modeling and Control: A Mechatronic Approach, John Wiley & Sons Ltd, 2014.

[19] J. C.Dixon, Suspension Geometry and Computation, A John Wiley and Sons Ltd, 2009.

[20] Z. S. R.M.Murray, A Mathematical Introduction to Robotic Manipulation, CRC Press, 1994.

[21] W. W. Shan, "http://mmu.ic.polyu.edu.hk/," Hong Kong Polytechnic University, [Online]. Available: http://mmu.ic.polyu.edu.hk/mu_proj/2012/IPD/IPD02%20Combine%20two%20Trikes%20into%20one%20HPV.htm. [Accessed 31 July 2016].

[22] R.C.Hibbeler, Engineering Mechanics: Dynamics 13th Edition, Pearson, 2013.

[23] S. S. R.Rajvardhan, "EFFECT OF WHEEL GEOMETRY PARAMETERS ON," *SASTECH Journal*, vol. 9, no. 2, pp. 11-18, 2010.

[24] U.-K.-K.-S. Sang-Ho, "Four-Wheel Independent Steering(4WIS) System for Vehicle Handling Improvement by Active Rear Toe Control," *JSME International Journal*, vol. 42, no. Series C, pp. 947-956, 1999.

[25] V. Cossalter, Motorcycle Dynamics, Second English Edition, Vittore Cossalter, 2006.

[26] National Highway Trafic Safeety Administration NHTSA technical report, "Trends in the Static Stability Factor of Passenger Cars, Light Trucks, and Vans," U.S. Department of Transportation , June 2005.

[27] National Highway Traffic Safety Administration NHTSA, "Initiatives to Address the Mitigation of Vehicle Rollover," NHTSA, 2003.

[28] H. B.Chen, "Differential-Braking-Based Rollover Prevention for," *Vehicle System Dynamics*, vol. 36, no. No 4-5, pp. 359-289, 2001.

[29] F. W. R.Azim, "Rollover Mitigation Controller Development for Three-Wheeled Vehicle Using Active Front Steering," *Mathematical Problems in Engineering,* vol. 2015, no. Article ID 918429, p. 9 pages, 2015.

[30] S.Yim, "Design of a robust controller for rollover prevention with active suspension and differential braking," *Journal of Mechanical Science and Technology,* vol. 26, no. No 1, pp. 213-222, 2012.

[31] Y. Y. A. M. J. Tan, "Cornering stabilty improvement by gyro moment for narow tilting vehicle," *Journal of Mechanical Science and Technology,* vol. 29, no. No 7, pp. 2705-2711, 2015.

[32] J. Wong, Theory of Ground Vehicles: Third Edition, John Wiley & Sons, Inc , 2001.

[33] R. Jazar, Vehicle Dynamics Theory and Application, NY. USA: Springer Science+Business Media, LLC, 2008.

[34] A. K. Avesta Goodarzi, *Lecture_8: Ride Dynamics,* Waterloo: University of Waterloo, 2015.

[35] D. R.Rajamani, "New Paradigms for the Integration of Yaw Stability and Rollover Prevention Functions in Vehicle Stability Control," *IEEE TRANSACTIONS ON INTELLIGENT TRANSPORTATION SYSTEMS,* vol. 14, no. No 1, pp. 249-261, 2013.

[36] R. G.Phanomachoeng, "Real-Time Estimation of Rollover Index for Tripped Rollovers With a Novel Unknown Input Nonlinear Observer," *IEEE/ASME TRANSACTIONS ON MECHATRONICS,* vol. 19, no. No 2, pp. 743-754, 2014.

[37] Fakhreddine O. Karray;Clarence W De Silva , Soft Computing and Intelligent Systems Design: Theory, Tools and Applications, Addison-Wesley, 2006.